Thermal Science and Engineering Progress 67 (2025) 104109

Contents lists available at ScienceDirect

Thermal Science and Engineering Progress

journal homepage: www.elsevier.com/locate/tsep

AI-assisted CFD energy and exergy analysis of turbulent natural convection of ternary hybrid nanofluids in a 3D open-ended enclosure with a wavy heated wall

Mohammad Abbaszadeh [a,*], Alireza Timas [b], Mohammad Ghalambaz [c,d]

[a] Hydro-Aeronautical Research Center, Shiraz University, Shiraz, Iran
[b] School of Mechanical Engineering, Shiraz University, Shiraz, Iran
[c] Department of Mathematical Sciences, Saveetha School of Engineering, SIMATS, Chennai, India
[d] Refrigeration and Air Conditioning Technical Engineering Department, College of Technical Engineering, The Islamic University, Najaf, Iraq

ARTICLE INFO

Keywords:
Natural convection
Ternary hybrid nanofluid
Wavy heated wall
Energy analysis
Rayleigh number (*Ra*)
Artificial neural network (ANN)

ABSTRACT

Passive cooling systems have attracted significant attention in recent years due to their cost-effectiveness and strong thermal performance. This study presents a detailed numerical investigation of steady-state natural convection in a three-dimensional open-ended cubic cavity featuring a wavy heated wall. The cavity is filled with ternary hybrid nanofluid composed of water (H_2O) as the base fluid and three types of nanoparticles: copper (Cu), copper oxide (CuO), and aluminum oxide (Al_2O_3). Buoyancy-induced fluid motion is modeled using the Boussinesq approximation. The governing equations for both laminar and turbulent flows are solved using the Reynolds-Averaged Navier–Stokes (RANS) method with the realizable k-ε turbulence model, following an experimentally validated approach. A parametric analysis examines the effects of Rayleigh number ($10^6 \le Ra \le 10^{12}$), nanoparticle volume fraction ($0\% \le \phi \le 5\%$), and the amplitude of wall waviness ($0\% \le A \le 30\%$) on thermal performance. The results reveal that incorporating wavy wall geometries in combination with nanofluids can substantially enhance the thermal performance of the system. Under certain optimized conditions, this configuration leads to a greater enhancement in heat transfer compared to the increase in entropy generation, resulting in a system efficiency exceeding unity. These findings highlight the strong potential of geometrically engineered surfaces for improving thermal transport in energy systems. To supplement the numerical results, an artificial neural network (ANN) was trained using the Levenberg–Marquardt algorithm on 72 datasets, accurately predicting average Nusselt numbers and validating the simulation trends as a fast and reliable predictive tool.

1. Introduction

In recent years, due to the limited availability of energy resources and their rising costs, the enhancement of energy efficiency has emerged as a primary objective within advanced technological research, particularly concerning thermal management systems such as heat exchangers. In this regard, natural convection within both closed and open cavities has received considerable attention owing to its broad range of industrial applications, including building technology, chemical processes, cooling equipment, nuclear power generation, and mine ventilation systems [1–3]. Improving heat transfer in such systems significantly contributes to enhanced operational efficiency and reduced energy consumption. Enhancement techniques are generally classified into passive techniques, which operate without the requirement of external power sources [4], and active methods, which depend on external energy inputs to augment heat transfer rates [5]. Due to the complex interaction between stationary fluids and thermal boundary layers, natural convection within cavities is recognized as a sophisticated phenomenon that necessitates extensive numerical and experimental analyses [6].

One of the widely discussed topics nowadays is the application of passive techniques in heat exchangers, particularly in open cavities. The primary reason for this is that these techniques do not require ongoing maintenance or incur additional costs. Furthermore, the simplicity associated with implementing these methods has encouraged engineers to prioritize passive techniques when aiming to enhance heat exchanger performance [7]. These techniques typically improve the thermal performance of heat exchangers by reducing thermal resistance through mechanisms such as promoting turbulence, enlarging

* Corresponding author.
E-mail address: Mabbaszadeh@shirazu.ac.ir (M. Abbaszadeh).

https://doi.org/10.1016/j.tsep.2025.104109
Received 6 May 2025; Received in revised form 1 September 2025; Accepted 12 September 2025
Available online 19 September 2025

Nomenclature

Acronyms

CFD	Computational Fluid Dynamics	Ra	Rayleigh number
Pr	Prandtl number	AI	Artificial Intelligence

Greek symbols

ϕ	Nanoparticle volume fractions, (%)	ρ	Density, (kg/m^3)
μ	Dynamic viscosity, (kg/ms)	ν	Kinematic viscosity, (m^2/s)
ν_t	Eddy viscosity, (m^2/s)	β	Thermal expansion coefficient, (1/K)
κ	Thermal conductivity, (W/mK)	κ_f	Thermal conductivity of base fluid, (W/mK)
α	Thermal diffusivity, (m^2/s)	σ	Electrical conductivity, (S/m)
γ	Specific heat ratio	T^*	Non-dimensional temperature
κ_{nf}	Thermal conductivity of nanofluid, (W/mK)		
κ_{hnf}	Thermal conductivity of hybrid nanofluid, (W/mK)		
κ_{thnf}	Thermal conductivity of ternary hybrid nanofluid, (W/mK)		
κ_{s1}	Thermal conductivity of nanoparticle CuO, (W/mK)		
κ_{s2}	Thermal conductivity of nanoparticle Cu, (W/mK)		
κ_{s3}	Thermal conductivity of nanoparticle Al_2O_3, (W/mK)		

Roman symbols

u	Velocity in the x-direction, (m/s)	v	Velocity in the y-direction, (m/s)
w	Velocity in the z-direction, (m/s)	u^*	Dimensionless velocity in x direction
v^*	Dimensionless velocity in y direction	p	Pressure, (Pa)
p^*	Dimensionless pressure	t^*	Dimensionless time
g	Gravitational acceleration, (m/s^2)	T	Temperature, (K)
C_p	Specific heat capacity, (J/kg K)	τ	Period of the wavy wall
A	Amplitude of the wavy heated wall (as a percentage of wall length)		

Subscripts

x	x-direction	f	Base fluid (water)
y	y-direction	nf	Nanofluid
z	z-direction	0	Cases with base fluid and non-wavy wall
$s1$	Nanoparticle 1 (CuO)	$thnf$	Ternary hybrid nanofluid
$s2$	Nanoparticle 2 (Cu)	hnf	Hybrid nanofluid
$s3$	Nanoparticle 3 (Al_2O_3)		

the effective heat transfer area, and modifying boundary layer characteristics. Among the most widely studied methods are twisted tape inserts, which induce swirl flows and enhance mixing within the flow field, leading to significant increases in the Nusselt number and overall thermal efficiency [8,9]. Baffles, particularly in helical, perforated, or V-shaped configurations, have also shown substantial benefits in flow reorganization and the elimination of stagnant zones, contributing to performance enhancements of up to 290% in some designs [10–12]. In addition to these methods, two passive strategies extended surfaces (fins) and nanofluids have drawn considerable attention for their flexibility, integration potential, and broad applicability across various thermal systems. Extended surfaces such as helical, corrugated, wavy, or louvered fins significantly increase the surface area available for convection, and studies have reported up to 56% enhancement in heat transfer performance using optimized fin geometries [13].

On the other hand, nanofluids, which are engineered by dispersing high-conductivity nanoparticles such as Al_2O_3, CuO, TiO_2, or graphene in base fluids, exhibit markedly improved thermal conductivity and convective heat transfer properties. Both mono and hybrid nanofluids have shown the potential to enhance thermal performance by 30%–70% depending on particle concentration and flow conditions [14,15]. Due to their adaptability and high efficiency, these two approaches offer significant potential for further investigation, especially in practical applications involving space constraints, high thermal loads, or compact heat exchanger designs, such as those addressed in the present work.

Rectangular and cubic-shaped geometries represent highly common and practical configurations encountered extensively in various industrial applications and have thus been the subject of numerous analytical and numerical investigations, both in two- and three-dimensional contexts. A review of the literature reveals that heat transfer and flow phenomena in enclosures are strongly influenced by the size of the opening. Bilgen and Muftuoglu [16] and Fontana et al. [17] extensively reported an enhancement in heat transfer with increasing cavity opening size, and conducted comprehensive numerical analyses to investigate a square open cavity with uniform heating, in order to clearly assess the effects of opening ratio and Rayleigh number (Ra) on natural convection heat transfer.Similarly, Elsayed et al. [18] and Abhinav et al. [19] performed a numerical study of natural convection in an open cavity with an internal heat source, focusing on the influence of ventilation locations, cavity aspect ratio, inclination angle, and the Grashof number (Gr). Complementing these efforts, Hussein and Mustafa [20] numerically analyzed natural convection in a fully open parallelogrammic cavity filled with Cu–water nanofluid under localized bottom heating, showing that cavity inclination and heat-source position jointly regulate the circulation patterns and overall heat-transfer response. Additional investigations on square-shaped open cavities with constant heat flux applied to the vertical wall were carried out by Polat and Bilgen [21] to evaluate the effects of inclination angle, cavity aspect ratio, non-dimensional wall thickness, thermal conductivity ratio, and Ra. More recent, Santos et al. [22] investigated steady-state laminar natural convection in a laterally heated, side-open cavity filled with a square lattice of solid blocks. Their findings emphasize the dominance of natural convection in complex geometries involving viscoplastic fluids. Additionally, Biswal and Meshram [23] explored the effects of aspect ratio and wall inclination in irregular cavity shapes on heat transfer and entropy generation in nanofluid-filled enclosures. Moreover, Gangawane et al. [24] conducted detailed research on the

influence of heat source aspect ratio in square cavities using the Lattice Boltzmann Method (LBM), showing that with increasing Prandtl number (from 0.71 to 7), the isotherms became more confined and the heat transfer rate increased linearly, with water yielding the highest Nusselt numbers. Sanjari et al. [25] presented foundational insights into the role of porous media in enhancing heat transfer within inclined cavity configurations. Their work highlights the importance of optimizing porous block placement relative to the heated wall and cavity openings.

Among the various geometrical modifications studied in the context of natural convection, open cavities with three-dimensional effects and wavy or corrugated heated walls represent a critical area of investigation due to their practical relevance and the complex flow structures induced by wall topology such as irregular cavity shape or wall roughness profile [26]. These configurations can result in significant alterations in the velocity field, formation of recirculation zones, and enhanced surface interactions, thereby influencing heat transfer characteristics. Several studies have reported that the introduction of surface undulations, especially in 3D domains, leads to intensified local mixing and non-uniform heat flux distributions, contributing to higher thermal performance. However, despite their significance, many existing studies have focused predominantly on two-dimensional analyses, which may fail to capture the inherently three-dimensional nature of the flow and heat transfer in such geometries [27–29]. Therefore, exploring natural convection in 3D open cavities with corrugated boundaries remains an essential and underexplored domain, as addressed in the present work.

One of the widely used approaches in computational fluid dynamics (CFD) is the application of the Navier–Stokes equations, which play a crucial role in the analysis of heat and mass transfer phenomena. For instance, Hansda et al. [30] investigated thermosolutal convection in a wavy-walled enclosure at $Ra = 10^6$ and $Le = 2$ using a Cu–water nanofluid. They employed the Navier–Stokes equations in conjunction with the KKL model proposed by Kleinstreuer and Feng [31] to incorporate the effects of Brownian motion of nanoparticles on thermophysical properties, using a H_2O/Cu nanofluid as the working medium. Their results indicated that the addition of nanoparticles enhances heat transfer while reducing mass transfer. Other relevant research areas include the investigation of the effects of convexity and concavity of vertical walls in rectangular wavy enclosures under various thermal and concentration conditions. Moreover, studying the influence of mechanical vibrations on a Cu-Al_2O_3/H_2O nanofluid inside a porous enclosure with partial heating, which is an area with significant applications in the electronics industry, is also of considerable research interest [32,33]. In the following review of the literature, the study by Li et al. [34] can be highlighted, in which natural convection of a water-based (Al_2O_3) nanofluid in a square-shaped enclosure was investigated. They considered the effects of Rayleigh number, power-law index, and nanoparticle characteristics and observed that heat transfer improves with increasing Rayleigh number and nanoparticle volume fraction, while it decreases with higher power-law index values. Using the same square cavity configuration, Hossain et al. [35], as well as Hossain and Molla [36], employed the MRT-LBM method to examine the natural convection of ethylene glycol-(Al_2O_3) power-law nanofluid in the presence of adiabatic fins. Their findings consistently revealed that increasing the nanoparticle volume fraction (ϕ) leads to an enhancement in the average heat transfer rate and total entropy generation, particularly at lower power-law index values.

Despite the remarkable capabilities of conventional numerical methods like CFD, their computational cost and limitations in handling complex, nonlinear systems have led researchers to explore data-driven alternatives. Machine learning, recognized as one of the core domains within Artificial Intelligence (AI), aims to enhance prediction accuracy by simulating human learning processes through the use of algorithms and data. Artificial Neural Networks (ANNs) have demonstrated remarkable capabilities in modeling complex and nonlinear systems, particularly in fields such as fluid mechanics, heat transfer, and related disciplines. These models, trained using data derived from Computational Fluid Dynamics (CFD) simulations or experimental measurements, can accurately predict key thermal performance indicators such as temperature distribution, Nusselt number, entropy generation, and overall thermal efficiency often at a significantly lower computational cost compared to traditional methods. Consequently, ANN-based models are increasingly employed either as powerful complements to or effective surrogates for high-fidelity simulations, accelerating optimization processes, parametric studies, and thermal system design. In the context of natural convection in enclosures containing various nanoparticle compositions, several studies have shown that ANN models are capable of successfully predicting heat transfer behavior under diverse boundary conditions and fluid properties. This highlights the strong potential of ANNs for future modeling applications in thermal engineering [37,38]. For instance, Panda et al. [39] integrated a feedforward ANN with response surface methodology to model nonlinear heat transfer in 3D micropolar nanofluids. The ANN accurately predicted thermal behavior, confirming its effectiveness in complex thermofluid analysis. Similarly, Wang et al. [40] combined artificial neural computing with statistical techniques to analyze melting heat and mass transport in magneto-viscous nanofluid flows. Their model, trained on Runge–Kutta-generated data, successfully captured the effects of thermal stratification, activation energy, and Brownian motion, highlighting the value of ANN-based approaches in advanced heat transfer modeling. In a related study, Sultan et al. [41] utilized an ANN model trained on 7838 data points to optimize phase change heat transfer in metal-foam-filled enclosures, revealing that increasing porosity from 0.9 to 0.975 can reduce melting time by up to 66%. Likewise, Aljibori et al. [42] employed an ANN-finite element framework to model MHD heat transfer in NEPCM-filled enclosures, successfully capturing the effects of magnetic fields and thermal parameters on entropy generation with high accuracy and efficiency.

While data-driven models offer promising advancements, recent numerical studies continue to refine conventional techniques for specific scenarios. For example, Cengizci et al. [43] employed the SUPG/PSPG finite element method to simulate nanofluid-filled square cavities and showed that their stabilized formulation remained accurate and stable up to Rayleigh numbers of 10^6 and $\phi = 0.2$, with CuO nanofluid yielding the highest heat transfer. Building upon prior investigations of square enclosures, Jelita and Saleh [27] conducted a numerical study on heat transfer performance in cavities filled with water-based nanofluids combined with nano-encapsulated phase change materials (NEPCM). Their research compared three different wall configurations standard, elastic, and open to assess the influence of wall type and nanoparticle volume fraction on the flow structure and thermal behavior. The findings revealed that alterations in wall geometry, particularly the incorporation of corrugated surfaces, significantly enhance flow disturbance and intensify non-uniformities within the velocity field. These effects, in turn, contribute to localized improvement in heat transfer performance, highlighting the effectiveness of geometrical modifications as a passive strategy for thermal enhancement [28,29,44,45].

However, focusing on the research gap reveals that, none of the previous studies in the literature have thoroughly examined the effects of high Rayleigh numbers, where the flow transitions into a three-dimensional nature due to increased turbulence in the flow field. Moreover, most existing research on square enclosures has focused on two-dimensional simulations using various methods, and only a few studies have addressed the three-dimensional flow behavior in the presence of wavy walls. It should be noted that sinusoidal topography has potential benefits in terms of imposing periodic contraction and expansion that thins thermal boundary layers, strengthens shear, and generates topography-induced secondary vortices, while also modulating ambient inflow and outflow in open cavities. Accordingly, the objectives of the present study is to conduct a comprehensive three-dimensional investigation of open-ended square enclosures with wavy

walls, focusing on the effects of hybrid nanofluids an innovative subject that has received limited attention in the existing literature. In addition to conventional numerical analysis, an ANN model is developed and trained on simulation data to predict key thermal performance indicators under varying conditions. This hybrid numerical-AI approach not only reduces computational cost but also enhances generalization capabilities for parametric studies. The research explores the interaction between thermal and solutal gradients in the presence of hybrid nanoparticles and their influence on natural heat transfer within an open-ended cubic cavity. Furthermore, the effects of wavy wall amplitude across different Rayleigh numbers and nanoparticle volume fractions are systematically analyzed. This study addresses critical gaps in understanding these phenomena and provides valuable insights for applications in energy systems, material processing, and other industrial domains. The primary motivation behind this work is to enhance the efficiency of cooling systems widely used in advanced engineering and industrial applications. It must be emphasized that the problem of natural convection in 3D wavy enclosures has real-world applications in passive cooling of electronic enclosures and heat sinks with wavy walls, etc.

The remainder of this paper is organized as follows: Section 1 presents a comprehensive overview of the current state of research on natural convection in open-ended cavities, with an emphasis on passive heat transfer enhancement techniques, particularly the application of hybrid nanofluids and geometrical modifications such as wavy walls. Section 2 outlines the physical problem, including the geometric configuration, boundary conditions, and mathematical formulation, along with the effective thermophysical properties of the hybrid nanofluid. Section 3 discusses the mesh sensitivity study and validates the numerical model against benchmark solutions to ensure accuracy. The computational results, including local and global thermal performance metrics under various Rayleigh numbers, nanoparticle volume fractions, and wall oscillation amplitudes, are analyzed in detail in Section 4, where an ANN model is also employed to predict key thermal responses based on the numerical dataset. Finally, the main conclusions and potential implications of the findings are summarized in Section 5.

2. Problem statement and mathematical representation

A schematic illustration of the physical model is presented in Fig. 1, which includes two unstructured polyhedral mesh configurations for the studied cavity flows. The computational domain consists of a three-dimensional open-ended square cavity with a length (L), height (H), and width (W), each equal to 0.5 m, resulting in an aspect ratio of 1. Building on this geometric specification, the fundamental assumptions underpinning the mathematical formulation are delineated explicitly. In the present analysis, the temperature distribution of the hot wavy wall is considered uniform; the working fluid is treated as Newtonian and incompressible with steady-state flow, and constant thermophysical properties are assumed for both the base fluid and the nanoparticles. Since the flow within the cavity is buoyancy-driven, the Boussinesq approximation is employed to model natural convection accurately. The governing equations are discretized using the finite-volume method. All simulations are carried out in STAR-CCM+, which is well suited to multiphysics and heat-transfer applications. Accordingly, the present study aims to generate high-fidelity numerical data that can serve as a benchmark for future investigations of natural-convection phenomena. To this end, a thermally active wavy wall with variable amplitudes ranging from 0% to 30% of the cavity length is implemented to induce geometric complexity. In addition, this type of water-based nanofluid, namely those containing copper (Cu), copper oxide (CuO), and aluminum oxide (Al_2O_3) nanoparticles, are considered in order to examine the influence of nanoparticle composition on heat transfer characteristics. The simulations are performed across both laminar and turbulent flow regimes, and a parametric analysis is carried out to evaluate the effect of nanoparticle volume fractions (ranging from 0% to 5%) on the enhancement of natural convective heat transfer within the enclosure.

2.1. Geometric configuration and boundary conditions

To establish a rigorous numerical framework, the boundary conditions defining the thermal and flow characteristics of the system are introduced in the following section. The top, bottom, front, and back walls are adiabatic with no-slip conditions, ensuring zero velocity and no heat flux normal to the surface. The left wall is maintained at a fixed temperature and follows a no-slip condition, acting as the primary heat source. The right wall functions as a pressure outlet, where the pressure is set to $p = p_{out}$ and velocity gradients are zero in the normal direction. A complete set of boundary conditions is detailed in Table 1. As illustrated in Fig. 1, the wavy wall is defined by a constant period (τ) and a variable ($A\%$), which ranges from 0% to 30% of the cavity length (L).

2.2. Fundamental equations

The governing equations are introduced in this Section 2.2, with the Reynolds-Averaged Navier–Stokes (RANS) equations formulated to encompass a comprehensive spectrum of flow regimes, including laminar, transitional, and turbulent states. The equations are discretized using the finite volume method to ensure local conservation and numerical stability. To integrate the buoyancy-induced force into the vertical (axial) component of the momentum equation, the Boussinesq approximation is invoked. This approximation, which maintains a high degree of accuracy under low to moderate thermal intensities, presupposes that fluid properties remain invariant, except for density perturbations driven by temperature gradients, thereby facilitating the representation of the buoyancy force term [48,49].

The governing equations of fluid motion consist of the continuity, momentum, and energy equations, each of which describes a fundamental aspect of the flow dynamics. The first fundamental equation is the continuity equation, which ensures mass conservation in the system. For a three-dimensional steady-state flow with the mixture model (m) utilized in this research, it is expressed as:

$$\frac{\partial u_{i,m}}{\partial x_i} = 0 \tag{1}$$

where $u_{i,m}$ represents the velocity components in the three Cartesian directions (u, v, w), while x_i denotes the corresponding spatial coordinates (x, y, z), ensuring mass conservation in a steady-state incompressible flow.

Following the mass conservation principle, the next fundamental equation governing the fluid motion is the momentum equation. This equation describes the balance of inertial, pressure, viscous, and buoyancy forces in the system and is formulated as:

$$\frac{\partial \left(u_{j,m} u_{i,m}\right)}{\partial x_j} = -\frac{\partial P_m}{\partial x_i} + \frac{1}{Re}\left(\frac{\partial^2 u_{i,m}}{\partial x_j \partial x_j}\right) + \frac{Gr}{Re^2} T^* \tag{2}$$

where $u_{i,m}$ and $u_{j,m}$ represent the velocity components in the three Cartesian directions (u, v, w), while x_i and x_j denote the corresponding spatial coordinates (x, y, z). P_m is the dimensionless pressure field, Re is the Reynolds number, and Gr is the Grashof number. The term $\frac{1}{Re}\left(\frac{\partial^2 u_{i,m}}{\partial x_j \partial x_j}\right)$ represents the diffusive effects due to viscosity, while $\frac{Gr}{Re^2} T^*$ accounts for the influence of buoyancy forces in the momentum transport equation.

To fully describe the thermal transport mechanisms in the system, the energy equation must also be considered. This equation accounts for both convective and diffusive heat transfer and is given as:

$$\frac{\partial \left(u_{j,m} T^*\right)}{\partial x_j} = \frac{1}{\mathrm{RePr}}\left(\frac{\partial^2 T^*}{\partial x_j \partial x_j}\right) \tag{3}$$

where T^* represents the dimensionless temperature field, $u_{j,m}$ denotes the velocity components in the three Cartesian directions (u, v, w), and x_j corresponds to the spatial coordinates (x, y, z). The term RePr is the

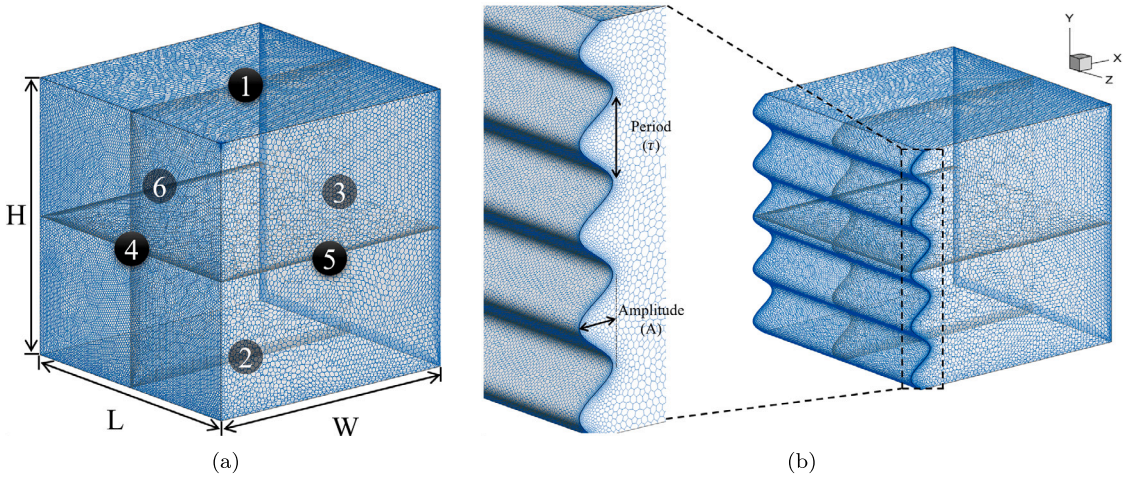

Fig. 1. Unstructured mesh representations for two geometrical configurations. (a) Shows the domain configuration with a cubical cavity and labeled boundary surfaces. (b) Illustrates a wavy-walled cavity with sinusoidal geometry, where the (A) is defined as a percentage of the wall length, and the period (τ) characterizes the wavelength.

Table 1
Boundary conditions for the open-ended cavity flow problem.

Wall specification		Boundary condition	Equation
Number	Position		
1	Top (Adiabatic)	No-slip, adiabatic	$u = v = w = 0, \quad \frac{\partial T}{\partial z} = 0$
2	Bottom (Adiabatic)	No-slip, adiabatic	$u = v = w = 0, \quad \frac{\partial T}{\partial z} = 0$
3	Right (Outlet)	Pressure outlet, fixed temperature	$p = p_{\text{out}}, \quad \frac{\partial u_i}{\partial x} = 0, \quad T^* = 0.0$
4	Left (Heat Source)	No-slip, fixed temperature	$u = v = w = 0, \quad T^* = 1.0$
5	Front (Adiabatic)	No-slip, adiabatic	$u = v = w = 0, \quad \frac{\partial T}{\partial y} = 0$
6	Back (Adiabatic)	No-slip, adiabatic	$u = v = w = 0, \quad \frac{\partial T}{\partial y} = 0$

Table 2
Thermophysical properties of base fluid and nanoparticles [43,46,47].

Property	Unit	Base Fluid (H_2O)	Nanoparticles		
			Cu	CuO	Al_2O_3
Specific heat (C_p)	J/kg K	4179	385	531.8	765
Thermal conductivity (k)	W/m K	0.613	401	76.5	40
Density (ρ)	kg/m^3	997.1	8933	6320	3970
Thermal expansion (β)	K^{-1}	2.761×10^{-4}	1.67×10^{-5}	1.8×10^{-5}	0.85×10^{-5}
Dynamic viscosity (μ)	N s/m^2	8.550×10^{-4}	–	–	–
Thermal diffusivity (α)	m^2/s	1.463×10^{-7}	1.17×10^{-4}	–	–

product of the Reynolds number (Re) and the Prandtl number (Pr), which characterizes the relative importance of momentum and thermal diffusivities in the flow.

For cases involving turbulent flow, an appropriate turbulence model must be employed to account for the additional transport of momentum and energy due to turbulent fluctuations. In the present study, the realizable $k-\varepsilon$ model is selected to properly model turbulence, as it offers superior performance in capturing recirculation zones and vortex formation, remains robust across a wide range of Rayleigh numbers, and is widely used and recommended by many investigators [50,51]. These equations, which characterize the turbulent viscosity and energy dissipation within the system, are expressed in [52]. In conjunction with the turbulence modeling, the accurate prediction of flow and heat transfer characteristics also relies heavily on the proper evaluation of the nanofluid's thermophysical properties. Specifically, to accurately capture the behavior of the ternary hybrid nanofluid under study, the effective thermophysical properties are evaluated based on the volume fractions and intrinsic characteristics of the constituent materials. It should be noted that while this model has is extensively used in the literature [53–55] and has shown adequate accuracy in most cases, these equations have some potential shortcoming of particle order dependency and accuracy. Therefore, in future studies more accurate relationships for computations of thermophysical properties is expected. The following relations describe the density, heat capacity, viscosity, thermal expansion coefficient, and thermal conductivity of the (Cu-CuO-Al_2O_3)/H_2O nanosuspension introduced in Table 2:

$$\rho_{\text{thnf}} = (1-\phi_3)\left\{\left[(1-\phi_2)\left((1-\phi_1)\rho_f + \phi_1\rho_{s1}\right)\right] + \phi_2\rho_{s2}\right\} + \phi_3\rho_{s3} \tag{4}$$

$$\left(\rho c_p\right)_{\text{thnf}} = (1-\phi_3)\left\{\left[(1-\phi_2)\left((1-\phi_1)(\rho c_p)_f + \phi_1(\rho c_p)_{s1}\right)\right] + \phi_2(\rho c_p)_{s2}\right\} + \phi_3(\rho c_p)_{s3} \tag{5}$$

$$\mu_{\text{thnf}} = \mu_f\left[(1-\phi_1)(1-\phi_2)(1-\phi_3)\right]^{-2.5} \tag{6}$$

$$(\rho\beta)_{\text{thnf}} = (1-\phi_3)\left\{\left[(1-\phi_2)\left((1-\phi_1)(\rho\beta)_f + \phi_1(\rho\beta)_{s1}\right)\right] + \phi_2(\rho\beta)_{s2}\right\} + \phi_3(\rho\beta)_{s3} \tag{7}$$

$$\kappa_{\text{thnf}} = \kappa_{\text{hnf}} \cdot \frac{\kappa_{s3} + 2\kappa_{\text{hnf}} - 2\phi_3(\kappa_{\text{hnf}} - \kappa_{s3})}{\kappa_{s3} + 2\kappa_{\text{hnf}} + \phi_3(\kappa_{\text{hnf}} - \kappa_{s3})} \tag{8}$$

where κ_{hnf} and κ_{nf} are given by:

$$\kappa_{\text{hnf}} = \kappa_{\text{nf}} \cdot \frac{\kappa_{s2} + 2\kappa_{\text{nf}} - 2\phi_2(\kappa_{\text{nf}} - \kappa_{s2})}{\kappa_{s2} + 2\kappa_{\text{nf}} + \phi_2(\kappa_{\text{nf}} - \kappa_{s2})} \tag{9}$$

Table 3
Grid independence study analyzing the influence of mesh resolution on the accuracy of thermal and flow characteristics for an oscillating wall cavity at different grid densities.

A	Ra	ϕ	Nu_{avg}	S_{gen}	Number of elements	Deviation (%)	
						Nu_{avg}	S_{gen}
10.0	1.0×10^{10}	0.0	222.0214	0.075774	36 545	18.12	22.29
10.0	1.0×10^{10}	0.0	271.1583	0.097514	73 089	15.34	18.23
10.0	1.0×10^{10}	0.0	320.2952	0.119254	358 857.0	0.54	3.52
10.0	1.0×10^{10}	0.0	322.0198	0.123608	707 165.0	–	–

$$\kappa_{\mathrm{nf}} = \kappa_f \cdot \frac{\kappa_{s1} + 2\kappa_f - 2\phi_1(\kappa_f - \kappa_{s1})}{\kappa_{s1} + 2\kappa_f + \phi_1(\kappa_f - \kappa_{s1})} \tag{10}$$

Here, the subscript f refers to the base fluid (water), while s_1, s_2, and s_3 denote the solid nanoparticles CuO, Cu, and Al_2O_3, respectively. The total volume fraction of the nanoparticles is represented by ϕ, with $\phi = \phi_1 + \phi_2 + \phi_3$. In this study, the nanoparticles are assumed to be equally distributed, such that $\phi_1 = \phi_2 = \phi_3 = \phi/3$.

3. Grid convergence analysis and model validation

3.1. Grid sensitivity analysis

A comprehensive grid sensitivity analysis is crucial for ensuring the accuracy and stability of numerical simulations, particularly in fluid dynamics studies. The objective of this study is to assess the impact of mesh resolution on the numerical solution's convergence, reducing discretization errors and achieving mesh independence while maintaining computational efficiency. In this investigation, a grid refinement study has been performed for an oscillating-wall cavity problem at $Ra = 10^{10}$ and $\phi = 0.0\%$. The computational domain was discretized using progressively refined mesh sizes corresponding to element counts of 36 545, 73 089, 358 857, and 707 165, as shown in Table 3. The sensitivity analysis was conducted by evaluating the average Nusselt number (Nu_{avg}) and entropy generation (S_{gen}), as these parameters are critical in assessing heat transfer and thermodynamic irreversibility, respectively.

From Table 3, it is evident that as the grid resolution increases, the variations in Nu_{avg} and S_{gen} diminish. The relative deviation of Nu_{avg} and S_{gen} between 73 089 and 358 857 elements is 15.34% and 18.23%, respectively, whereas between 358 857 and 707 165 elements, the deviations reduce significantly to 0.54% and 3.52%. This confirms that the solution becomes nearly grid-independent beyond 358 857 elements, indicating that further refinement yields only marginal improvements. To ensure a balance between computational cost and solution accuracy, a mesh resolution of 358 857 elements is adopted for all subsequent simulations. The final grid configuration is selected to minimize computational overhead while maintaining numerical precision. Moreover, the average Nusselt number is formulated as follows:

$$Nu_{ave} = \frac{1}{\zeta}\int_0^{\zeta} Nu_y \, d\zeta \tag{11}$$

Here, $Nu_y = h_y D/k$ is the local Nusselt number in the y-direction. This expression quantifies the rate of convective heat transfer at the wall surface, normalized by the conductive heat transfer across the fluid. The local convective coefficient h_y is determined based on the temperature gradient at the solid–fluid interface and is a function of the wall geometry and fluid properties. The average Nusselt number, as highlighted in the present study, represents a key metric for evaluating thermal performance, where increases in its value signify improved natural convection resulting from the combined effects of wall surface waviness and the enhanced thermophysical properties of hybrid nanofluids.

To evaluate the irreversibility associated with heat and momentum transfer in the system, the volumetric entropy generation rate is also calculated. Entropy generation analysis offers a thermodynamic perspective on the efficiency of the heat transfer mechanism, highlighting the sources of energy degradation within the flow. The total entropy generation rate per unit volume is given by [56]:

$$\begin{aligned}\dot{S}'''_{\mathrm{gen}} = \dot{S}'''_{\mathrm{gen,H}} + \dot{S}'''_{\mathrm{gen,V}} = {} & \frac{k_{thnf}}{T^2}\left[\left(\frac{\partial T}{\partial x}\right)^2 + \left(\frac{\partial T}{\partial y}\right)^2 + \left(\frac{\partial T}{\partial z}\right)^2\right] \\ & + \frac{\mu_{nf}}{T}\left[2\left(\left(\frac{\partial u}{\partial x}\right)^2 + \left(\frac{\partial v}{\partial y}\right)^2 + \left(\frac{\partial w}{\partial z}\right)^2\right)\right. \\ & + \left(\frac{\partial u}{\partial y} + \frac{\partial v}{\partial x}\right)^2 + \left(\frac{\partial u}{\partial z} + \frac{\partial w}{\partial x}\right)^2 \\ & \left. + \left(\frac{\partial v}{\partial z} + \frac{\partial w}{\partial y}\right)^2\right]\end{aligned} \tag{12}$$

In this formulation, the first term corresponds to the thermal irreversibility due to temperature gradients, while the second term accounts for viscous dissipation caused by velocity gradients in the flow field. The integration of $\dot{S}'''_{\mathrm{gen}}$ over the domain yields the total entropy generation rate, S_{gen}, which is a key parameter in evaluating the thermodynamic cost of heat transfer enhancement methods. Lower entropy generation indicates more efficient thermal systems with reduced irreversible losses, thus reflecting the effectiveness of the adopted passive enhancement techniques. To express the local entropy generation in a dimensionless form, the entropy generation number N_G is defined as $N_G = (\dot{S}'''_{\mathrm{gen}} l^2)/k_f$, where $\dot{S}'''_{\mathrm{gen}}$ is the volumetric entropy generation rate, l is the characteristic length, and k_f is the thermal conductivity of the base fluid.

Finally, by integrating the dimensionless form over the heated part of the domain, the average entropy generation number N_s is computed as

$$N_s = N_{s,H} + N_{s,V} = \int N_G \, dv \tag{13}$$

3.2. Numerical code verification and validation

Validation is a critical aspect of any numerical study, ensuring that the computational results accurately represent the underlying physical phenomena. In the context of buoyancy-driven flows, validating a numerical approach against established benchmarks provides confidence in the predictive capability of the method. To enhance the robustness and credibility of the validation process, this study incorporates comparisons with two well-recognized benchmark investigations: the work by Mohamad et al. [57], which utilizes the Lattice Boltzmann Method (LBM), and the study by Jahanshahi et al. [58], which focuses on natural convection in nanofluids using experimentally measured thermal conductivities.

The problem under investigation involves buoyancy-driven flow within open cavities, where the interplay between internal recirculatory flow and the external environment significantly influences the heat transfer characteristics. Both reference studies provide valuable insights into the convective behavior of fluids under thermally stratified conditions. In particular, the study by Jahanshahi et al. [58] employs H_2O/SiO_2 nanofluid and incorporates a two-dimensional laminar free convection model within a square cavity. The governing equations are formulated using the Boussinesq approximation, and the thermophysical properties of the nanofluid are modeled using two approaches: experimental measurement of effective thermal conductivity using the transient hot-wire method, and theoretical estimation based on the Hamilton-Crosser model.

These dual approaches allow for a direct evaluation of uncertainty in the thermal modeling of nanofluids. The fluid is assumed to behave as a single-phase homogeneous medium, and the results demonstrate significant differences in heat transfer predictions depending on the

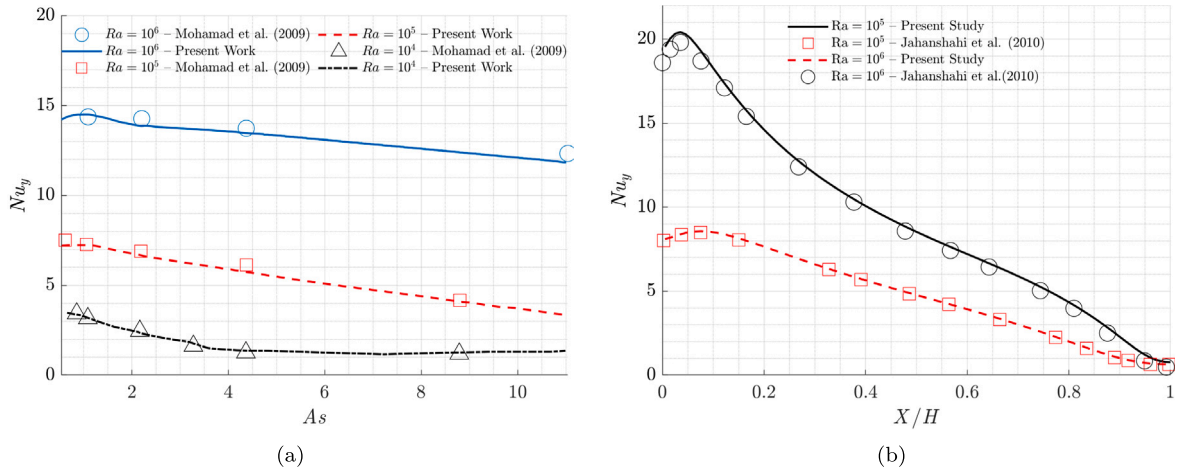

Fig. 2. Comparison of the local Nusselt number (Nu_y) for different Rayleigh numbers ($Ra = 10^4, 10^5, 10^6$) among the present work and Mohamad et al. [57] and Jahanshahi et al. [58], along with the relative error percentage.

choice of conductivity model. The computational results presented in that study include temperature contours, streamline patterns, and average Nusselt numbers for various Rayleigh numbers ($Ra = 10^5, 10^6, 10^7$) and nanoparticle volume fractions ($\phi = 0$ to 4%). In the present work, simulations are conducted under identical geometric and boundary conditions to those used in both [57,58]. However, key differences exist in the numerical discretization schemes and the treatment of boundary conditions, which directly affect the stability and precision of the solutions. The current methodology employs a refined finite-volume approach capable of resolving sharp velocity and thermal gradients, especially in regions of high convective intensity. The comparative analysis of average Nusselt numbers across different Rayleigh numbers ($Ra = 10^4, 10^5, 10^6$) demonstrates that the present model closely follows the trends observed in the reference studies, with improved accuracy in capturing flow structures and thermal fields. Notably, the consistency with the results based on experimental thermal conductivity models from [58] (as shown in Fig. 2(b)) validates the effectiveness of the current computational framework in modeling nanofluid behavior under natural convection conditions. As illustrated in Figs. 2(a) and 2(b), for $Ra = 10^6$, the present method shows strong agreement with both references, with relative errors below 6%. For $Ra = 10^5$ and $Ra = 10^4$, minor deviations are observed, primarily due to differences in numerical resolution and turbulence modeling, yet the results remain within acceptable error margins.

The current approach is based on the single-phase mixture model and the governing equations include continuity, momentum, and energy balances solved in an steady-state three-dimensional framework. A realizable k-ε turbulence model is used to represent turbulent transport, with user-defined source terms set to zero. Turbulent viscosity, buoyancy forces, and energy dissipation terms are evaluated using validated constants from prior literature. Overall, the inclusion of both theoretical and experimental benchmarks particularly the experimentally-backed nanofluid modeling from [58] substantially reinforces the validity of the present numerical approach. The observed alignment in Nusselt number trends and thermal distribution patterns confirms the robustness and accuracy of the proposed method in analyzing buoyancy-driven heat transfer in open cavity configurations.

4. Computational results and interpretation

4.1. CFD-based results

This study with the view to systematically investigate the effects of water-based nanofluids containing ternary or triple nanoparticles, in conjunction with nanoparticle volume fraction (ϕ), A, and Ra, on natural convective heat transfer enhancement within an open cavity under steady-state conditions. Building upon this framework, an extensive parametric analysis is conducted to evaluate the combined influence of wall geometry and nanoparticle composition on convective heat transfer performance. In the first step of analyzing the case of a simple undulated 3D cavity investigated which serves as the reference for performance evaluations the hybrid nanofluid with water as the base fluid, and examined the variations of the average Nusselt number and entropy generation across different Rayleigh numbers for varying volume fractions of nanoparticles including ternary nanofluid, without oscillation of the hot wall. As observed in Table 4, increasing the nanoparticle volume fraction consistently enhances the average Nusselt number. At $Ra = 10^6$, the Nusselt number increases by approximately 10.75% from 16.944 to 18.764 as ϕ rises from 0% to 5%. Similarly, at $Ra = 10^8$, a 10.37% enhancement is observed, while at $Ra = 10^{10}$, the increase reaches about 12.27%. At the highest Rayleigh number, $Ra = 10^{12}$, the improvement amounts to approximately 16.54%. It is also noteworthy that while the enhancement in the Nusselt number becomes more pronounced with higher Rayleigh numbers, the entropy generation exhibits a significant upward trend as well. Although the addition of nanoparticles boosts heat transfer, it also increases the thermodynamic cost of the system, reflected in the rise of irreversibility. Moreover, it can be observed that at lower Rayleigh numbers, the rate of increase in the Nusselt number is faster than that of entropy generation, suggesting an efficient thermal improvement with relatively minor penalties in entropy production. However, at extremely high Rayleigh numbers ($Ra = 10^{12}$), entropy generation accelerates sharply, almost surpassing the relative growth in the Nusselt number. This highlights that at very high convection intensities, the system becomes significantly more irreversible despite the continued improvement in heat transfer. This initial investigation provides a fundamental basis for the dimensionless analysis in the next phase of the study, establishing a comprehensive framework to scale and generalize the results for broader thermal engineering applications.

The second step in the analysis focuses on the results illustrated in Fig. 3, which shows the behavior of the local Nusselt number (Nu_y) along midplane line of the heated wall at a fixed Rayleigh number of 10^6 and in the absence of nanoparticles ($\phi = 0\%$). The figure presents a comparison across multiple wavy wall amplitudes (A). For the flat wall case ($A = 0\%$), Nu_y illiterates a mild declining trend. As the wall amplitude increases, Nu_y displays periodic oscillations, with pronounced peaks in contraction regions and lower values in expansion zones. These variations are primarily driven by the interaction of the fluid flow with the wavy boundaries specifically, the thinning of the thermal boundary layer in constricted regions and the emergence of

Table 4
The average Nusselt number and entropy generation for various Rayleigh numbers and volume fractions of ternary hybrid nanofluid at zero wall amplitude ($A = 0.0\%$).

Ra	Nu_{avg}			S_{gen}		
	$\phi = 0\%$	$\phi = 2\%$	$\phi = 5\%$	$\phi = 0\%$	$\phi = 2\%$	$\phi = 5\%$
10^6	16.944	17.646	18.764	9.76×10^{-11}	1.15×10^{-10}	1.49×10^{-10}
10^8	60.879	63.260	67.198	3.00×10^{-6}	3.57×10^{-6}	4.64×10^{-6}
10^{10}	222.071	232.650	249.313	8.73×10^{-2}	1.03×10^{-1}	1.34×10^{-1}
10^{12}	939.027	1000.288	1094.417	972.071	1084.129	1269.188

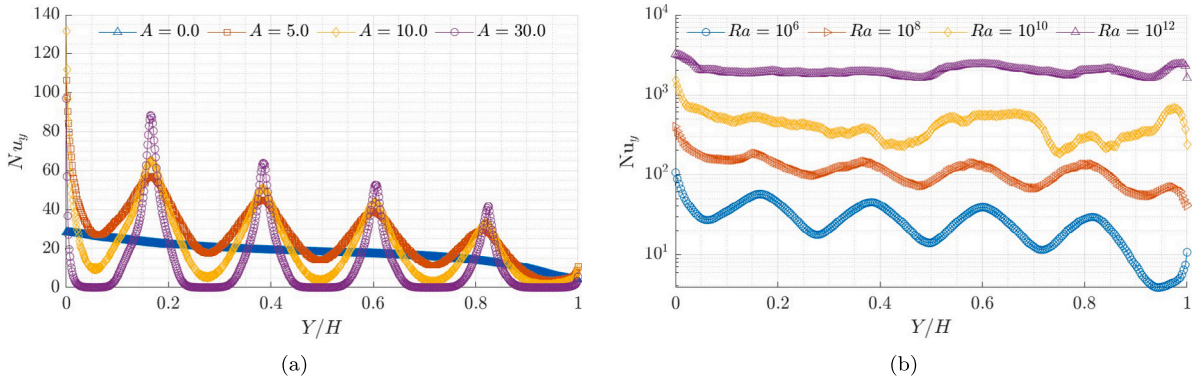

Fig. 3. Comparison of the local Nusselt number (Nu_y) for different wall oscillation amplitudes (A) at a constant $Ra = 10^6$ and $\phi = 0\%$.

recirculation zones in wider segments. The magnitude of oscillations increases with wave amplitude, reaching a peak above 90 at $A = 30\%$. This behavior is attributed to enhanced shear layers and the intensified convective mixing induced by secondary vortical structures. When comparing the results for $A = 10\%$ and $A = 20\%$, it is evident that higher amplitudes yield more significant variations in local heat transfer, reflected in sharper peaks and more pronounced high/low Nu_y zones. Subsequent sections further explore the influence of ternary nanofluid on the thermal performance under various combinations of Ra, A, and ϕ, offering a detailed assessment of how nanoparticle material properties affect the overall heat transfer behavior in the system.

Moreover, Fig. 4 further explores the impact of wall oscillation amplitude and nanoparticle concentration by presenting the normalized Nusselt number $\overline{Nu}_{ave}$ across varying Rayleigh numbers. Fig. 4(a) ($A = 0\%$) reveals that in the absence of oscillations, higher nanoparticle concentrations $\phi = 5\%$ significantly enhance heat transfer compared to pure fluid $\phi = 0\%$, with $\phi = 2\%$ achieving an intermediate improvement. This behavior contrasts with the efficiency trends in Fig. 6, highlighting how thermal conductivity enhancement dominates Nusselt number performance despite viscosity penalties. As oscillations are introduced at $A = 1\%$ and $A = 5\%$, Figs. 4(b) and 4(c), all cases show increased heat transfer, with $\phi = 5\%$ consistently outperforming both $\phi = 2\%$ and pure fluid configurations. This suggests that even mild oscillations enhance convective mixing sufficiently to suppress viscosity effects and leverage the improved thermal conductivity of higher nanoparticle concentrations. The effect becomes more pronounced at $A = 10\%$ and $A = 20\%$ Figs. 4(d) and 4(e), where the gap between $\phi = 5\%$ and lower concentrations widens, indicating that stronger oscillations maximize the nanofluid's heat transfer potential. At the highest amplitude $A = 30\%$, Fig. 4(f), a significant leap in Nusselt number is observed across all configurations, with $\phi = 5\%$ achieving nearly 2.5 times the baseline heat transfer. This remarkable boost underscores the synergy between large-amplitude oscillations and high nanoparticle volume fractions, where enhanced thermal conductivity and intensified mixing collaboratively overcome viscosity-related limitations.

The results collectively emphasize that while increased nanoparticle concentrations generally improve heat transfer, the addition of wall oscillations particularly at higher amplitudes is crucial for unlocking the full potential of nanofluids, transforming their thermal performance beyond what is achievable by conductivity improvements alone. Fig. 5 examines normalized entropy generation $\overline{S}_{gen}$ versus Ra under varying nanoparticle volume fractions ϕ and wall oscillation amplitudes A. A general trend evident throughout all cases is that entropy generation systematically increases with nanoparticle concentration, especially pronounced at lower amplitudes and Rayleigh numbers, due to elevated thermal gradients and viscous dissipation. However, as oscillation amplitude increases, particularly at higher Rayleigh numbers, this effect is moderated. Fig. 5(a) $A = 0\%$ shows that entropy generation increases with nanoparticle concentration, with ($\phi = 5\%$) exhibiting the highest entropy production. This trend continues in Figs. 5(b) and 5(c) ($A = 1\%$ and $A = 5\%$), where higher nanoparticle fractions yield greater entropy generation, reflecting increased thermal gradients and viscous dissipation. With moderate oscillations $A = 10\%$ and $A = 20\%$, Figs. 5(d) and 5(e), entropy generation peaks at $Ra = 10^{10}$ before slightly decreasing, suggesting improved mixing reduces local temperature gradients, thus partly offsetting the entropy increase caused by nanoparticle concentration. In the final case $A = 30\%$, Fig. 5(f), entropy generation remains elevated but stabilizes at higher Rayleigh numbers, indicating oscillation-induced mixing effectively moderates entropy generation, balancing thermal performance and irreversibilities. Notably, this stabilization aligns closely with the previously observed enhancement in the $\overline{Nu}_{ave}$ (see Fig. 4), confirming that intensified oscillations foster uniform temperature distributions and suppress localized thermal gradients, reducing entropy production. This highlights the dual role of oscillations: enhancing heat transfer efficiency while controlling entropy generation at high amplitudes, thus improving overall thermodynamic performance.

Fig. 6 illustrates the variation of normalized efficiency η as a function of the Ra for different nanoparticle volume fractions $\phi\%$ and wall oscillation amplitudes $A\%$. Generally, η increases with Ra due to enhanced convective currents. Across all subfigures, a clear overall pattern emerges: while higher nanoparticle volume fractions $\phi = 5\%$ typically reduce efficiency due to increased viscosity and thermal resistance, significant recovery in efficiency is evident at high Rayleigh numbers and strong wall oscillations, indicating that vigorous convective mixing mitigates viscosity-related drawbacks and effectively leverages improved thermal conductivity. Interestingly, while ϕ =

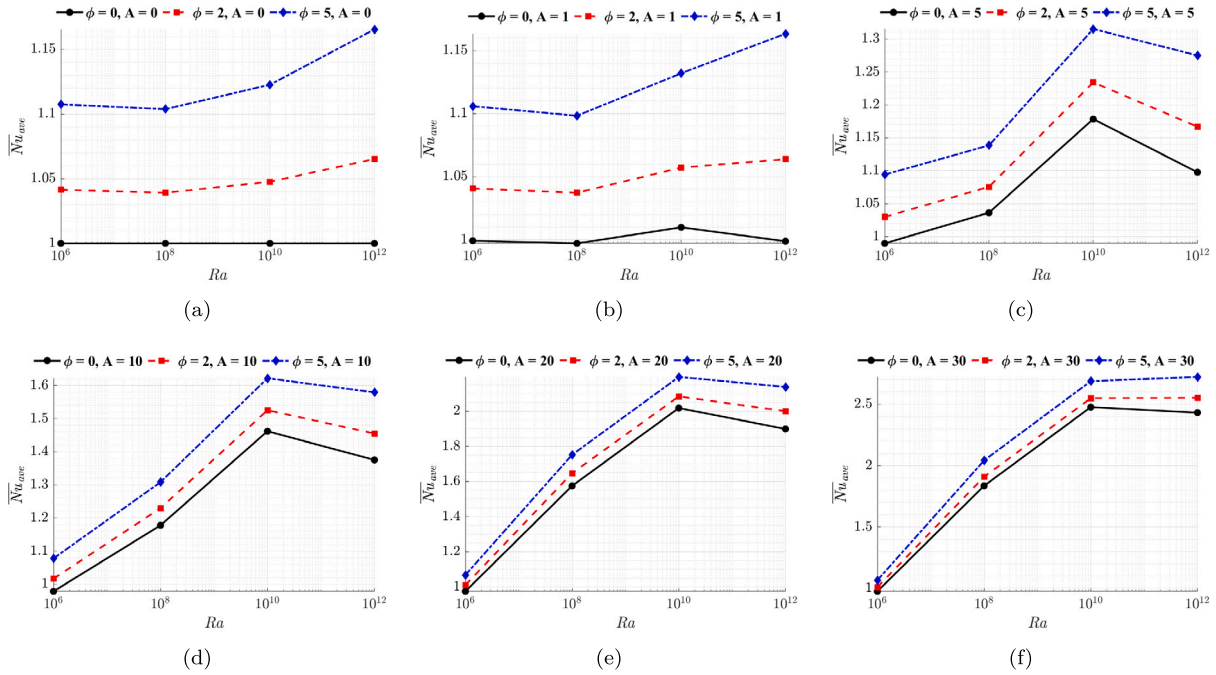

Fig. 4. Normalized average Nusselt number ($\overline{Nu}_{ave} = Nu_{ave}/Nu_{ave_0}$) versus Ra for different nanoparticle volume fractions ($\phi\%$) and wall oscillation amplitudes $A\%$.

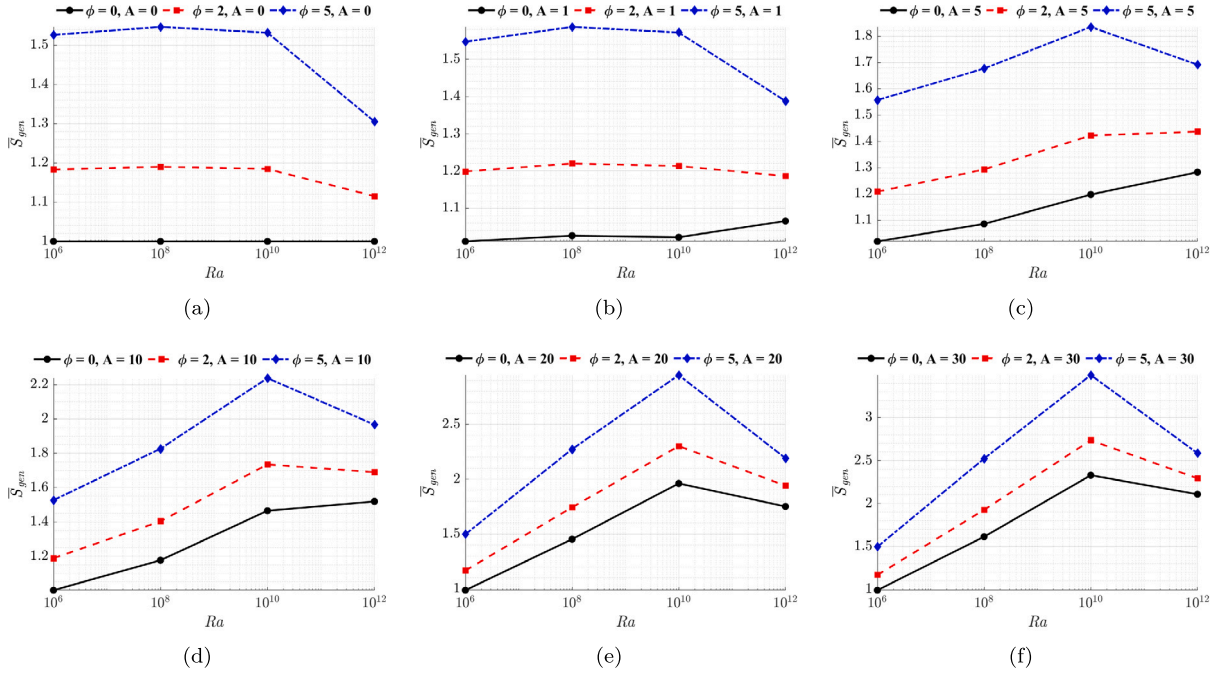

Fig. 5. Normalized entropy generation $\overline{S}_{gen} = S/S_0$ versus Rayleigh number for different nanoparticle volume fractions and wall oscillation amplitudes $A\%$.

5% continues to demonstrate the highest entropy generation due to increased viscosity and thermal resistance, the gap between $\phi = 5\%$ and lower concentrations ($\phi = 2\%$ and 0%) narrows at high oscillation amplitudes. This implies that strong oscillations mitigate some of the nanofluid's viscosity-induced entropy penalties, partially recovering efficiency losses. The comparison with Nusselt number trends further supports this observation, showing that the enhanced convective mixing driven by high-amplitude oscillations allows $\phi = 5\%$ to leverage its superior thermal conductivity more effectively. While the preceding entropy generation analysis reveals how oscillation amplitude and nanoparticle concentration jointly influence thermodynamic irreversibilities, it remains essential to explore how these parameters affect the internal thermal field and flow structure more directly. To this end, examining the temperature distribution and streamline patterns within the cavity provides deeper insight into the underlying transport mechanisms that govern entropy trends. Although increasing nanofluid concentration has gains in terms of systematic rise in heat-transfer capacity and stronger synergy with wall waviness, it should be that increasing this parameter above the level of 5% is not suggested due to risks of particles agglomeration and system instability.

Fig. 6(a) $A = 0\%$ serves as a baseline, demonstrating that the pure fluid case $\phi = 0\%$ consistently maintains the highest efficiency, while

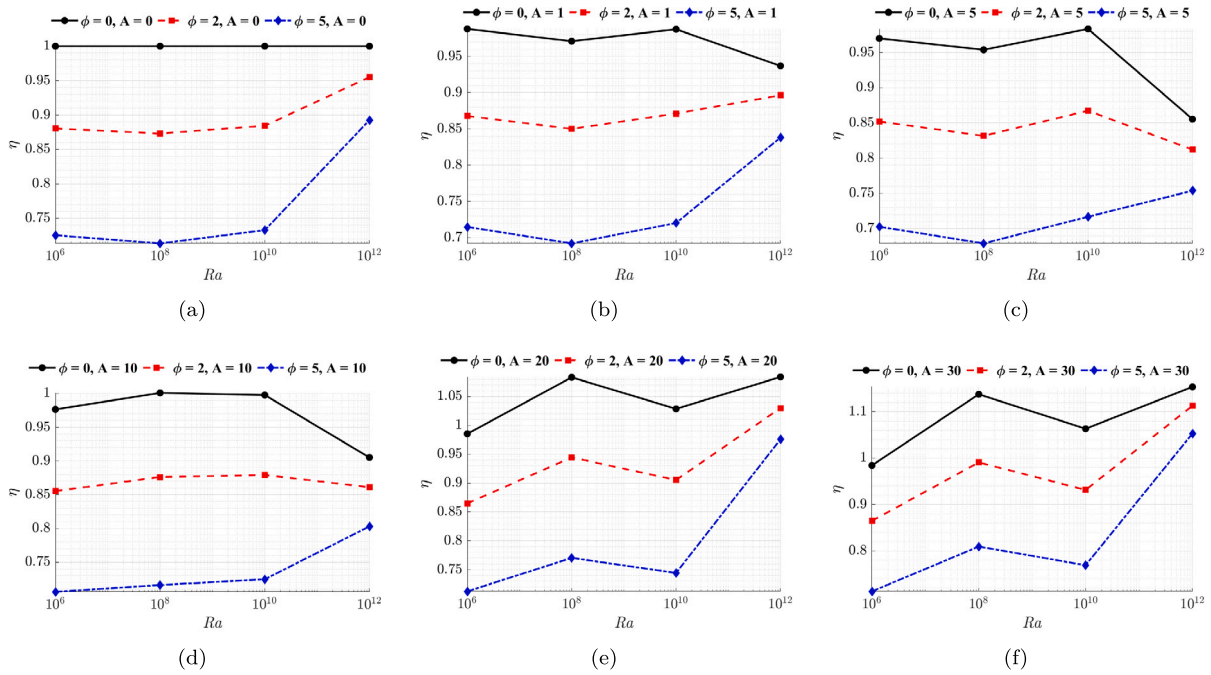

Fig. 6. Variation of the normalized efficiency η with the Ra for different nanoparticle volume fractions and wall oscillation amplitudes $A\%$.

increasing nanoparticle volume fractions to $\phi = 2\%$ and $\phi = 5\%$ reduces performance due to heightened viscosity, which suppresses convection despite the improved thermal conductivity of the nanofluid. A slight increase in amplitude to $A = 1\%$ Fig. 6(b) yields a minor efficiency improvement across all cases, although the hierarchy among volume fractions remains unchanged, suggesting that low-amplitude oscillations are insufficient to significantly disrupt the viscosity-driven thermal resistance. As the oscillation amplitude increases to $A = 5\%$ and $A = 10\%$ Figs. 6(c) and 6(d), a more pronounced shift emerges. The pure fluid case continues to lead in efficiency, but $\phi = 2\%$ demonstrates greater stability compared to $\phi = 5\%$, indicating that moderate nanoparticle concentrations strike a better balance between enhanced thermal conductivity and viscosity penalties. Notably, the efficiency for the pure fluid plateaus, while $\phi = 5\%$ starts to show a gradual recovery. This behavior implies that increasing oscillation amplitude fosters better mixing and thermal dispersion. The most striking behavior occurs at $A = 30\%$

Fig. 6(f), where the normalized efficiency exceeds unity for the pure fluid, signaling a super-efficiency regime driven by strong oscillations that significantly amplify convective heat transfer. $\phi = 2\%$ experiences a substantial efficiency rise, closely trailing the pure fluid case, while $\phi = 5\%$, though the least efficient overall, exhibits a notable recovery, reinforcing the hypothesis that higher oscillation amplitudes counteract viscosity-induced losses more effectively. Thus, the analysis clearly demonstrates that the key to maximizing the benefits of nanoparticle-enhanced fluids lies in applying sufficiently strong wall oscillations, which balance viscosity penalties and thermal conductivity enhancements to achieve optimal performance. These results underscore the pivotal role of wall oscillation amplitude in enhancing thermal efficiency, particularly at higher Rayleigh numbers. At the same time, they highlight the intricate trade-off between nanoparticle concentration and oscillation intensity. In the current analysis, the nanoparticle volume fraction is set to $\phi = 0\%$, which allows for an isolated assessment of the oscillation effects on flow and thermal behavior without the influence of particle-induced viscosity. Excessive nanoparticle loading, as will be discussed in the following sections, continues to degrade thermal performance unless it is accompanied by sufficiently strong oscillations to offset the adverse effects of increased viscosity. Moreover, a detailed investigation of the dimensionless temperature contours and streamlines across a wide range of Rayleigh numbers from 10^6 to 10^{12} and oscillation amplitudes ranging from 0 to 20 percent of the wall length, forms the central focus of the following section of this study.

As illustrated in Fig. 7, the streamlines and normalized temperature fields (T^*) are compared for four values of Rayleigh number ($Ra = 10^6$ to 10^{12}) and four amplitudes of hot wall oscillation ($A = 0, 5, 10, 20\%$). The comparison clearly demonstrates that the flow behavior and thermal response are strongly affected by both parameters. At $Ra = 10^6$, the flow remains steady and laminar, with symmetric and stable natural convection cells. Under these conditions, wall oscillation has minimal influence on the thermal field. As the Rayleigh number increases to $Ra = 10^8$, the flow enters a transitional regime, becoming more sensitive to wall oscillation. In this state, higher oscillation amplitudes lead to visible disruptions in the flow structure, thinner thermal boundary layers, and localized unsteadiness. In the fully turbulent regime ($Ra = 10^{10}$ and $Ra = 10^{12}$), the influence of wall oscillation becomes increasingly dominant. Larger oscillation amplitudes generate more intense vortex formations, sharper thermal gradients, and enhanced fluid mixing, all of which contribute to greater convective heat transfer rates. The interplay between buoyancy-induced turbulence and wall-driven oscillatory motion produces complex, non-symmetric flow patterns that are absent in lower Ra cases. These findings lay the groundwork for a deeper exploration into how nanoparticle concentration further modulates the observed thermal behavior. In particular, the next section investigates the case of $\phi = 5\%$ to determine how solid loading interacts with wall oscillation and buoyancy-driven flow at various Rayleigh numbers.

These findings lay the groundwork for a deeper exploration into how nanoparticle concentration further modulates the observed thermal behavior. In particular, the next section investigates the case of $\phi = 5\%$ to determine how solid loading interacts with wall oscillation and buoyancy-driven flow at various Rayleigh numbers. As shown in Fig. 8, the introduction of a 5% nanoparticle volume fraction significantly alters both the thermal and flow fields across the entire range of Rayleigh numbers. Compared to the $\phi = 0\%$ case, the presence of nanoparticles leads to a noticeable increase in thermal stratification and suppression of flow intensity, especially at lower oscillation amplitudes. This is primarily attributed to the enhanced effective viscosity and reduced thermal diffusivity of the nanofluid. At $Ra = 10^6$, the flow remains

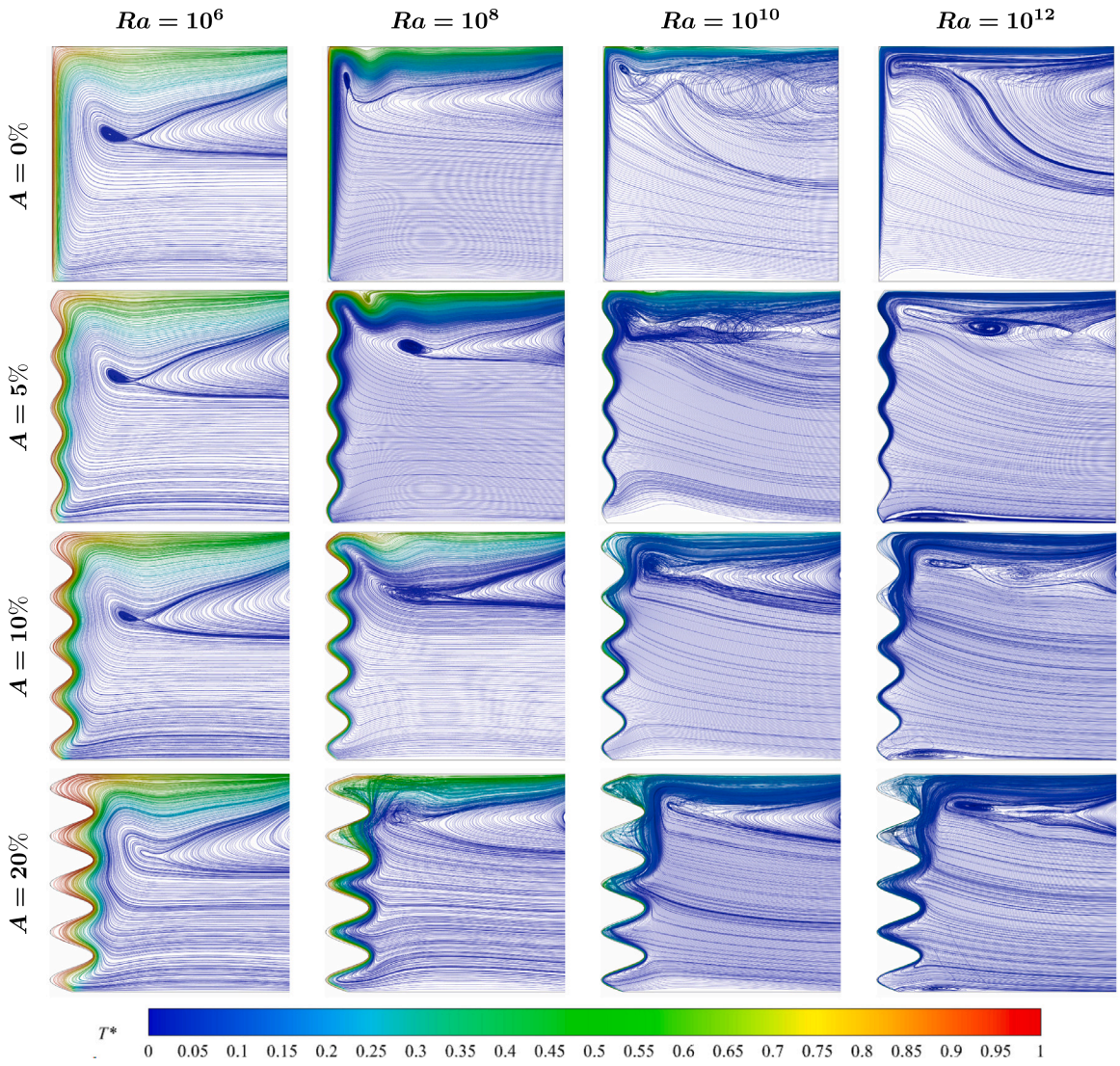

Fig. 7. Heat transfer characteristics and fluid flow patterns within the open-ended cavity at a wide range of ($Ra = 10^6$) to ($Ra = 10^{12}$), illustrating the influence of nanoparticle volume fraction at ($\phi = 0.0\%$) for different amplitudes of the wavy hot wall oscillation (A) ranging from 0% to 20%.

laminar and structured, but the thermal boundary layer thickens, and convective cells exhibit reduced circulation strength. In the transitional regime $Ra = 10^8$, the dampening effect of nanoparticles becomes more evident, with slower vortex formation and weaker mixing compared to the pure fluid case. In fully turbulent conditions ($Ra = 10^{10}$ and $Ra = 10^{12}$), although the flow regains complexity, the thermal boundary layers remain relatively thicker, and temperature gradients less sharp under low oscillation amplitudes. Interestingly, increasing the oscillation amplitude to $A = 20\%$ partially compensates for the negative impact of nanoparticle loading. Under strong oscillatory motion, the flow exhibits re-energized vortex structures, enhanced mixing near the heated wall, and improved heat transfer performance, highlighting the synergistic potential of combining nanoparticle enhancement with dynamic wall actuation. To further deepen the investigation, the analysis is extended to three-dimensional simulations, where the combined effects of wall oscillation and nanoparticle loading are evaluated at a volume fraction of $\phi = 2\%$. This transition to 3D geometry enables a more realistic depiction of the physical mechanisms governing thermoconvective transport, particularly in practical systems where out-of-plane effects significantly influence performance.

As depicted in Fig. 9, the dimensionless temperature contours (T^*) are shown on the central vertical planes of the cavity for three Rayleigh numbers ($Ra = 10^6$, 10^8, and 10^{12}) and three amplitudes of wall oscillation ($A = 0\%$, 10%, and 30%). These iso-contours provide a clear visualization of the thermal stratification, boundary layer development, and heat penetration depth under varying flow regimes and wall actuation intensities. At $Ra = 10^6$, where the flow remains laminar and conduction-dominated, the thermal boundary layer is relatively thick and stable across all oscillation amplitudes. Even at $A = 30\%$, the dimensionless temperature contours remain smooth and parallel, indicating limited enhancement in convective transport. However, small geometric deformation of the boundary layer adjacent to the wavy wall suggests the onset of mild thermal disturbances due to surface motion. In the transitional regime $Ra = 10^8$, wall oscillations begin to disrupt the thermal layering more noticeably. As A increases from 0 to 30, the isothermal contours bend and elongate into the cavity domain, signifying stronger wall-normal thermal transport and vortex development. This indicates that oscillatory wall motion facilitates deeper heat penetration by locally disturbing the buoyancy-stabilized thermal gradient. In the fully turbulent case ($Ra = 10^{12}$), dramatic changes are observed. At $A = 0\%$, thermal energy is confined near the wall, and the contours are tightly packed near the hot surface. As A rises to 10 and especially to 30, the thermal boundary layer becomes thinner, less uniform, and more fragmented. The T^* contours at $A = 30\%$ exhibit undulating patterns and extended thermal plumes into the

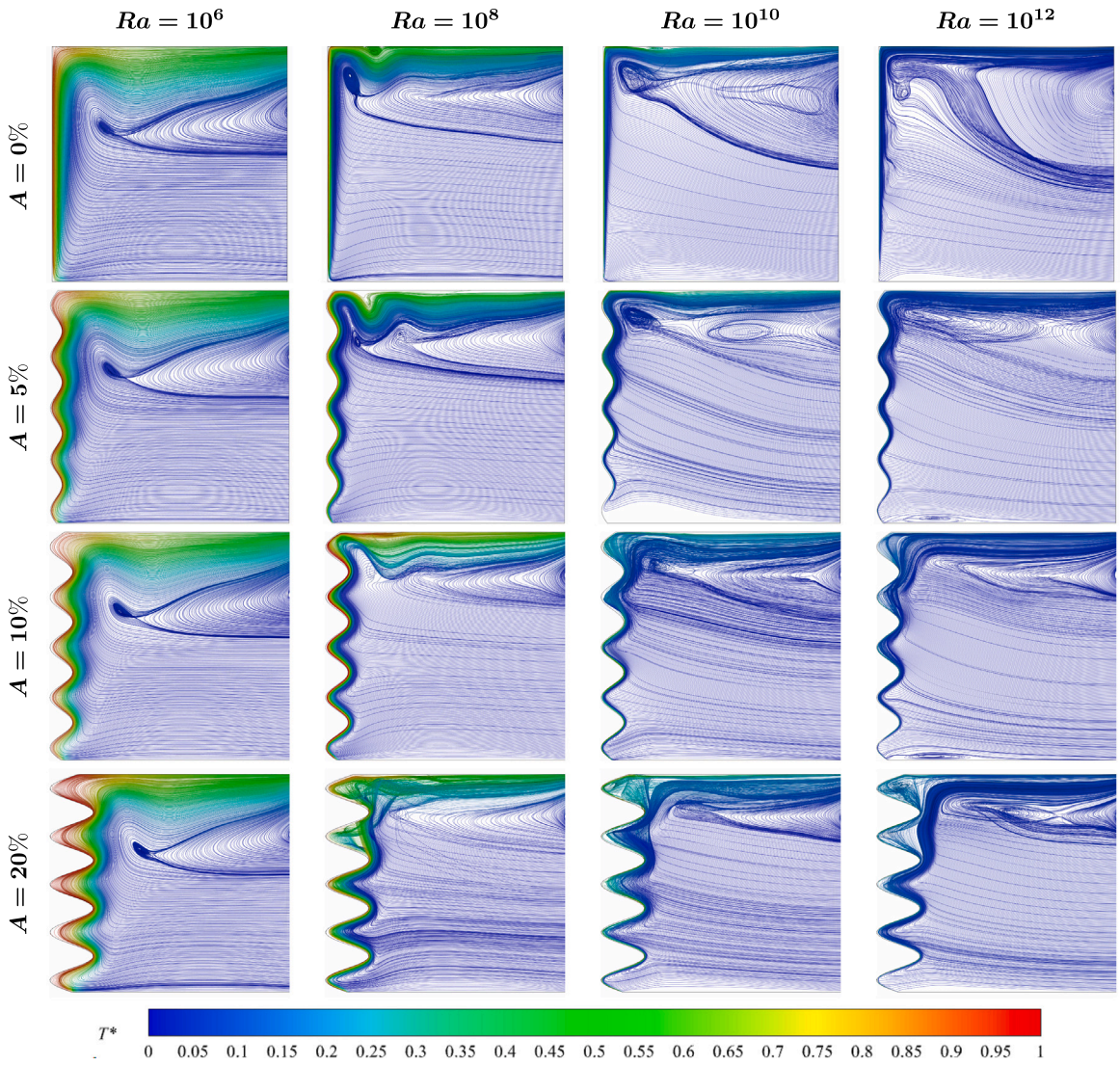

Fig. 8. Heat transfer characteristics and fluid flow patterns within the open-ended cavity at a wide range of $Ra = 10^6$ to $Ra = 10^{12}$, illustrating the influence of nanoparticle volume fraction at $\phi = 5.0\%$ for different amplitudes of the wavy hot wall oscillation A ranging from 0% to 20%.

cavity, which indicate enhanced mixing, turbulent advection, and significantly improved convective heat transfer. These three-dimensional results corroborate the 2D findings while also highlighting complex three-axis interactions that cannot be captured in planar analysis. The visual progression of thermal contour behavior affirms that wall oscillation, particularly at high amplitudes, acts as an active thermal control mechanism, intensifying both flow recirculation and heat dispersion, especially when combined with the modified thermophysical properties introduced by nanofluids. The obtained results reveals that the 3D characteristics of the flow at high Rayleigh number and high wavy amplitudes has negligible unsteady effects and therefore the steady state assumption is valid for all the cases.

4.2. ANN-based prediction

This Section 4.2 presents the development and implementation of an ANN model aimed at accurately predicting the average Nusselt number and thermal efficiency in a passive cooling system. The system under investigation consists of a three-dimensional open-ended cubic enclosure with a wavy heated wall, filled with ternary hybrid nanofluid composed of water (H_2O) as the base fluid and various metallic nanoparticles including copper (Cu), copper oxide (CuO), and aluminum oxide (Al_2O_3). The convective heat transfer is driven by buoyancy forces and governed by complex nonlinear interactions among key physical parameters such as the Rayleigh number, wall waviness amplitude, and nanoparticle volume fraction.

Due to the high computational cost and time associated with solving the governing equations especially over a wide range of Rayleigh numbers ($10^6 \leq Ra \leq 10^{12}$) the ANN approach is proposed as a data-driven alternative capable of capturing the underlying nonlinear behavior of the system. The model is designed with three input features (Ra, A, and ϕ) and two output targets: the $\overline{Nu}_{ave}$ and the overall thermal efficiency η. The application of ANN in this context offers several distinct advantages. It significantly reduces computational expense, effectively models intricate nonlinear relationships, and achieves high predictive accuracy, with a determination coefficient of R^2, indicating excellent agreement with numerical results. ANNs are brain-inspired algorithms designed to approximate complex nonlinear relationships between inputs and outputs. Common types of ANNs include: single-layer networks, multi-layer networks, feed-forward networks, and recurrent feed-forward networks. The selection of the number of neurons, the number of layers, and the proportion of data allocated for training, testing, and validation are among the key parameters that significantly influence the accuracy of the solution. Several researchers have conducted extensive studies to determine the

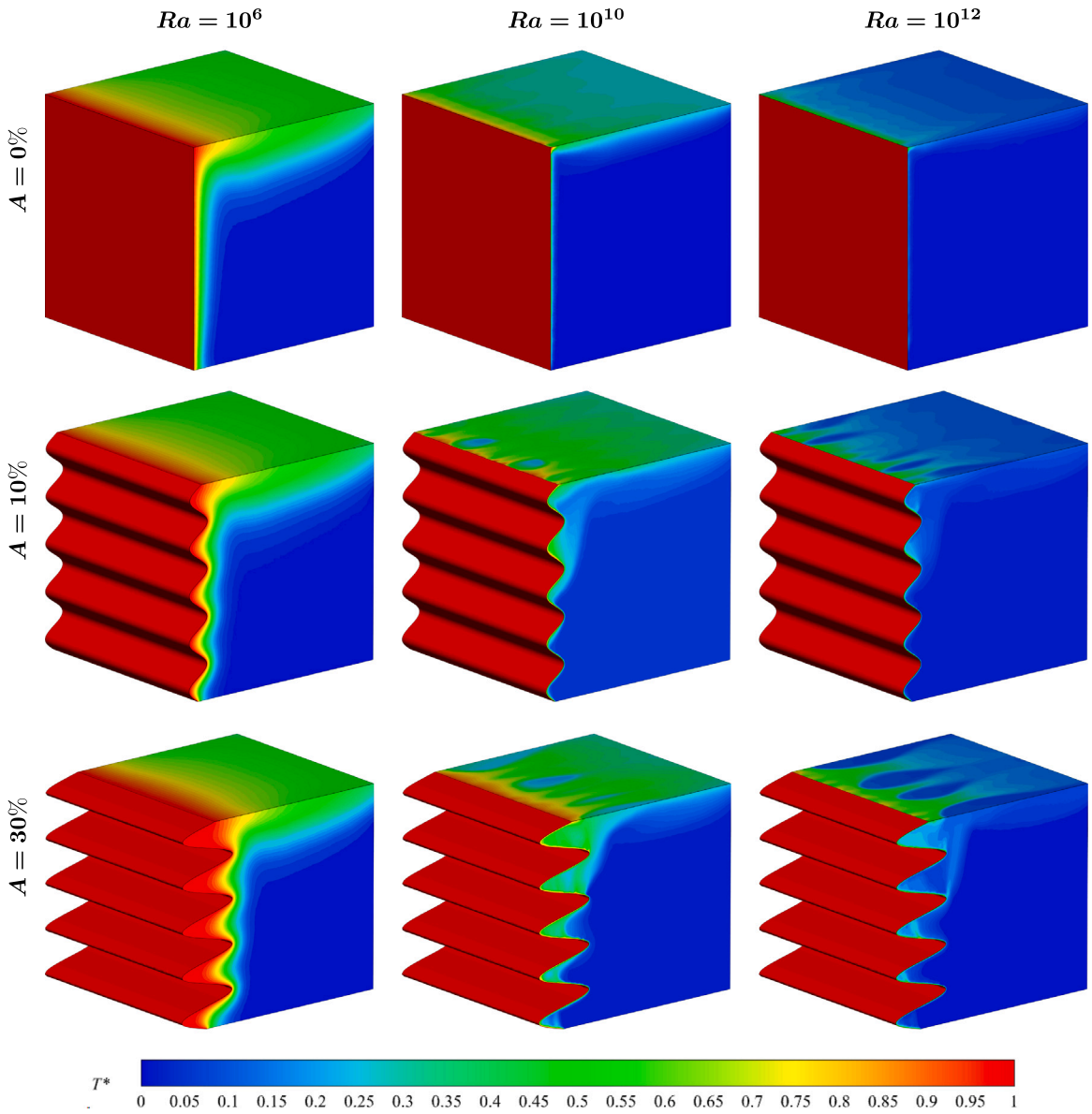

Fig. 9. Heat transfer and flow structures in an open-ended cavity for various $Ra = 10^6$ to 10^{12}, showing the effects of $\phi = 2.0\%$ and wall oscillation amplitudes $A = 0\%$, 10%, 30%.

appropriate number of neurons in the hidden layer. For instance, Alklaibi et al. [59] investigated the design of an ANN with 10 neurons in the hidden layer for predicting heat transfer. To prevent the issue of overfitting, the dataset was divided into three subsets: 86% for training, 7% for testing, and 7% for validation. Similarly, Rehman et al. [60] utilized an ANN model with 10 neurons in the hidden layer to examine the influence of various control parameters on the heat transfer coefficient. A total of 88 random samples were used, comprising 62 for training 70%, 13 for validation 15%, and 13 for testing 15%.

In current study, Fig. 10 illustrates a well-organized flowchart demonstrating how numerical results obtained from numerical programming have been transferred to the neural network model. As depicted, this research employs 10 neurons in the hidden layer and 2 neurons in the output layer, enabling accurate prediction of the average Nusselt number and thermal efficiency. To ensure effective learning and generalization of the network, a total of 72 data samples were utilized in the present study, systematically divided into 70% for training, 15% for validation, and 15% for testing. Furthermore, in this study, the network is trained using the Levenberg–Marquardt back propagation algorithm, ensuring robust generalization and predictive performance. In continuation of the conducted studies, a detailed evaluation has been performed for validation, training, and other related processes.

4.2.1. Comparative visualization of regression performance

In this Section 4.2.1, the performance of the feed-forward neural network was evaluated quantitatively using several statistical error metrics. The neural network employed the Levenberg–Marquardt back-propagation algorithm aimed at minimizing the Mean Squared Error (MSE) between the target and predicted values. The following metrics were selected to comprehensively assess the regression model: Root Mean Square Error (RMSE), Correlation Coefficient (R), Coefficient of Determination (R^2), Root Mean Relative Error (RMRE), and Mean Squared Error (MSE). These metrics are mathematically defined and briefly explained as follows [61]:

$$\mathrm{RMSE} = \sqrt{\frac{1}{2N}\sum_{i=1}^{N}\left\|\mathbf{y}_s^{(i)} - \mathbf{y}_a^{(i)}\right\|_2^2} \tag{14}$$

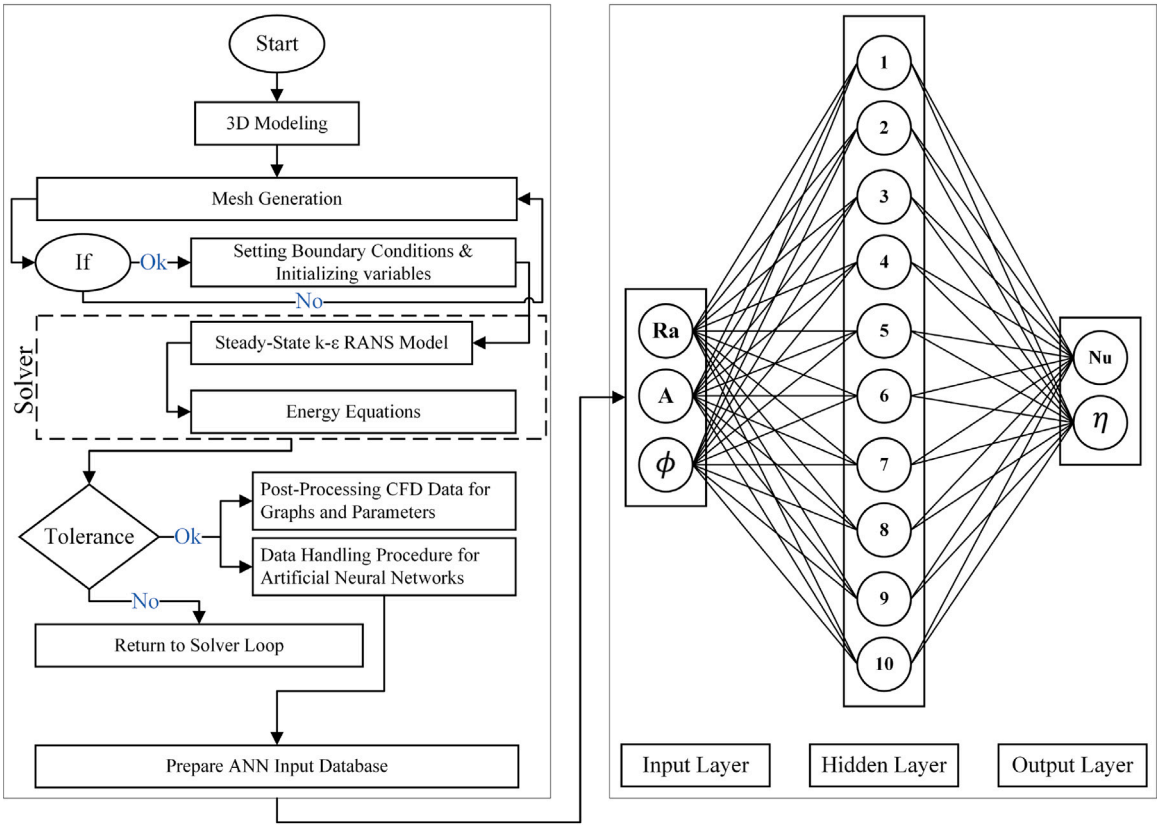

Fig. 10. Workflow of CFD-ANN integration and architecture of the employed feed-forward neural network.

where $\mathbf{y}_s^{(i)} = [\eta_{s,i}, Nu_{s,i}]^T$ and $\mathbf{y}_a^{(i)} = [\eta_{a,i}, Nu_{a,i}]^T$ are the true and predicted output vectors at sample i, respectively; $\overline{\mathbf{y}_s}$ and $\overline{\mathbf{y}_a}$ are the mean vectors of the true and predicted outputs; N is the number of samples.

$$R = \frac{\sum_{i=1}^{N}\left(\mathbf{y}_s^{(i)} - \overline{\mathbf{y}_s}\right)\cdot\left(\mathbf{y}_a^{(i)} - \overline{\mathbf{y}_a}\right)}{\sqrt{\sum_{i=1}^{N}\left\|\mathbf{y}_s^{(i)} - \overline{\mathbf{y}_s}\right\|_2^2 \sum_{i=1}^{N}\left\|\mathbf{y}_a^{(i)} - \overline{\mathbf{y}_a}\right\|_2^2}} \tag{15}$$

The correlation coefficient (R) measures the strength and direction of the linear relationship between predicted and actual outputs, with values closer to 1 indicating stronger positive correlation. Furthermore, the coefficient of determination (R^2) quantifies the fraction of variability in the actual outputs that can be explained by the input variables, where higher R^2 values reflect superior predictive performance. To complement these metrics, the RMRE provides a normalized evaluation of prediction accuracy by assessing the relative discrepancies between predicted and true outputs. The corresponding expressions for R^2 and RMRE are given as follows:

$$R^2 = 1 - \frac{\sum_{i=1}^{N}\left\|\mathbf{y}_s^{(i)} - \mathbf{y}_a^{(i)}\right\|_2^2}{\sum_{i=1}^{N}\left\|\mathbf{y}_s^{(i)} - \overline{\mathbf{y}_s}\right\|_2^2} \tag{16}$$

$$\mathrm{RMRE} = \sqrt{\frac{1}{2N}\sum_{i=1}^{N}\left(\left|\frac{\eta_{s,i} - \eta_{a,i}}{\eta_{s,i}}\right| + \left|\frac{Nu_{s,i} - Nu_{a,i}}{Nu_{s,i}}\right|\right)} \tag{17}$$

$$\mathrm{MSE} = \frac{1}{2N}\sum_{i=1}^{N}\left\|\mathbf{y}_s^{(i)} - \mathbf{y}_a^{(i)}\right\|_2^2 \tag{18}$$

MSE quantifies the average squared error between the predicted and actual outputs, with lower values indicating better model performance and generalization capability. In the present study, the trained ANN model achieved excellent predictive accuracy with $RMSE = 0.002791$, $R^2 = 0.99992$, $RMRE = 0.039163$. These statistical measures collectively provide a robust and comprehensive evaluation of the regression performance during both the training and validation phases. They ensure that the trained ANN model is not only accurate in predictions but also reliable and generalizable across unseen data. This ANN algorithm, as illustrated in Fig. 10, uses three inputs (Ra, ϕ, A) and two outputs (η and Nu_{ave}). A tan-sigmoid transfer function was used for the hidden layer, and a linear transfer function was used for the output layer.

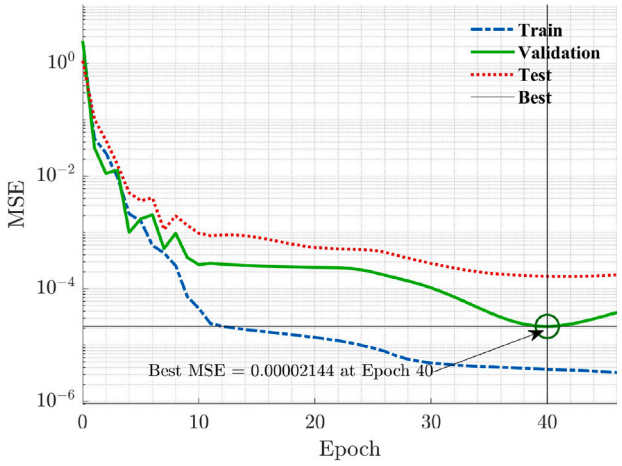

Fig. 11. Training history of MSE showing optimal validation performance (2.144×10^{-5}) achieved at epoch 40 with early stopping.

Furthermore, The training performance of this configuration is evaluated using the Mean Squared Error (MSE) metric. As shown in Fig. 11, the MSE performance of the model over 46 epochs is illustrated for the training, validation, and test datasets. The training error (blue

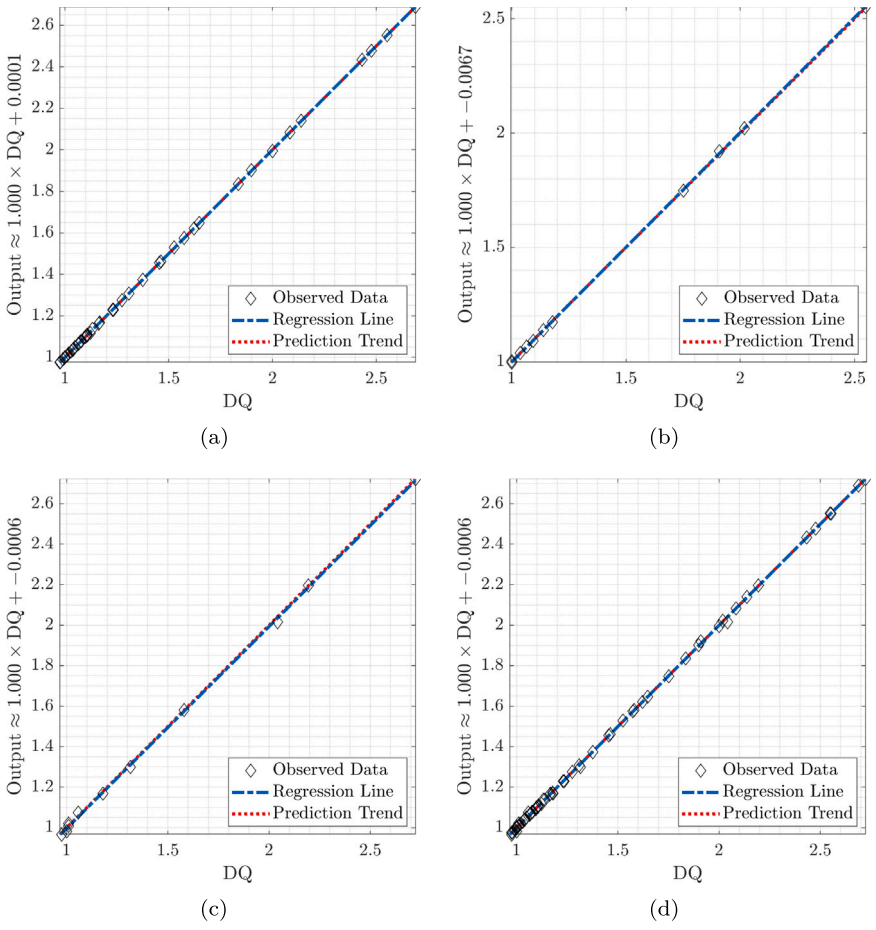

Fig. 12. Regression performance of the ANN model for predicting Nu_{ave} and η, with Desired Quantity (DQ) on the horizontal axis and predicted outputs on the vertical axis. Correlation coefficients (R) are: (a) training data R = 0.99999, (b) validation data R = 0.99997, (c) testing data R = 0.99979, and (d) the entire datasets R = 0.99994.

dashed line) shows a continuous decreasing trend, indicating that the network successfully learns the mapping between input and output variables. The validation error (green solid line) also decreases during the early stages of training and reaches its minimum value of 0.0.00002144 at epoch 40, after which it exhibits a slight increase. This behavior suggests the beginning of overfitting beyond this point, where the model starts to lose its generalization capability. The test error (red dotted line), although slightly higher than the training and validation errors, remains relatively stable throughout the epochs, confirming the acceptable generalization performance of the model. A black marker on the plot highlights the epoch corresponding to the best validation performance. Overall, the convergence behavior of the MSE curves demonstrates that the network has been efficiently trained and optimized, achieving a good balance between accuracy and generalizability. Fig. 12 illustrates the regression performance of the trained ANN model across different phases: training, validation, testing, and the entire dataset. The observed data points align closely with the regression and prediction trend lines in all subplots, indicating a high level of agreement between the model outputs and actual values. The correlation coefficients (R) for each phase are remarkably high 0.99999 for training, 0.99997 for validation, 0.99979 for testing, and 0.99994 for the complete dataset demonstrating the robustness and accuracy of the model in predicting both (Nu_{ave}) and (η). These results confirm the model's capability to generalize well beyond the training data and accurately capture the nonlinear relationships among the input and output parameters.

4.2.2. Analysis of predicted thermal characteristics by ANN model

The contour plots presented in Figs. 13 and 14 provide valuable insights into the thermal behavior of the system as predicted by the trained ANN model. Fig. 13 illustrates the distribution of the ($\overline{Nu}_{ave}$) as a function of Rayleigh number and the oscillation amplitude for three volume fractions of nanoparticles (ϕ = 0%, 2%, and 5%). As expected, an increase in Ra consistently leads to higher values of $\overline{Nu}_{ave}$, indicating enhanced convective heat transfer at stronger buoyancy-driven flows. Additionally, increasing A tends to improve heat transfer performance, particularly at moderate to high values of Ra, due to increased fluid mixing. The effect of nanoparticle concentration is also evident: as ϕ increases from 0% to 5%, the maximum values of $\overline{Nu}_{ave}$ increase, confirming the positive role of nanoparticles in enhancing thermal conductivity.

In contrast, Fig. 14 presents the contours of thermal efficiency (η) under the same parametric conditions. Unlike the trend observed in $\overline{Nu}_{ave}$, thermal efficiency shows a more complex behavior. The efficiency generally decreases with increasing Ra, particularly at higher oscillation amplitudes, due to increased pumping power requirements associated with stronger convection. Interestingly, the inclusion of nanoparticles slightly reduces the peak efficiency zones, suggesting that while heat transfer improves, the overall thermodynamic efficiency may be compromised due to higher energy input requirements. This trade-off highlights the importance of optimizing system parameters based on both thermal performance and energy efficiency. Overall, the ANN-based predictions successfully capture the nonlinear interplay between Ra, A, and ϕ, offering a reliable surrogate modeling framework for rapid thermal performance assessments without the need for

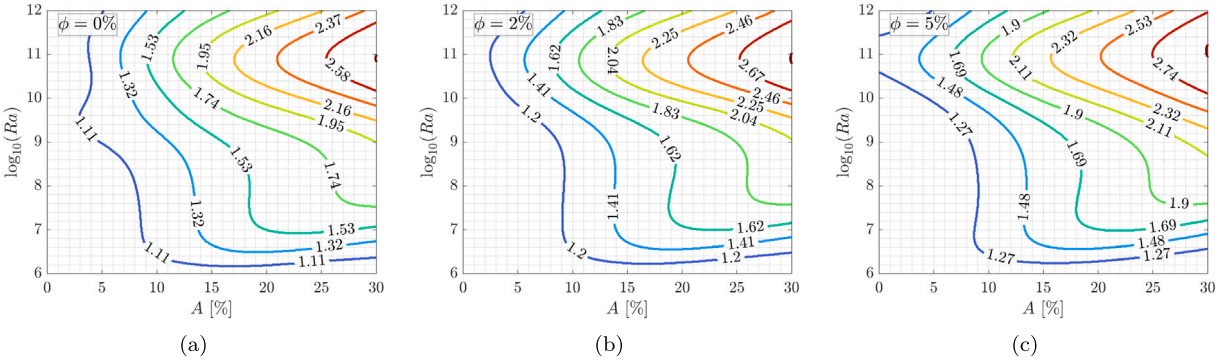

Fig. 13. Contours of normalized average Nusselt number $\overline{Nu}_{ave}$ as functions of Ra and A for $\phi = 0\%$ to 5%, based on ANN predictions.

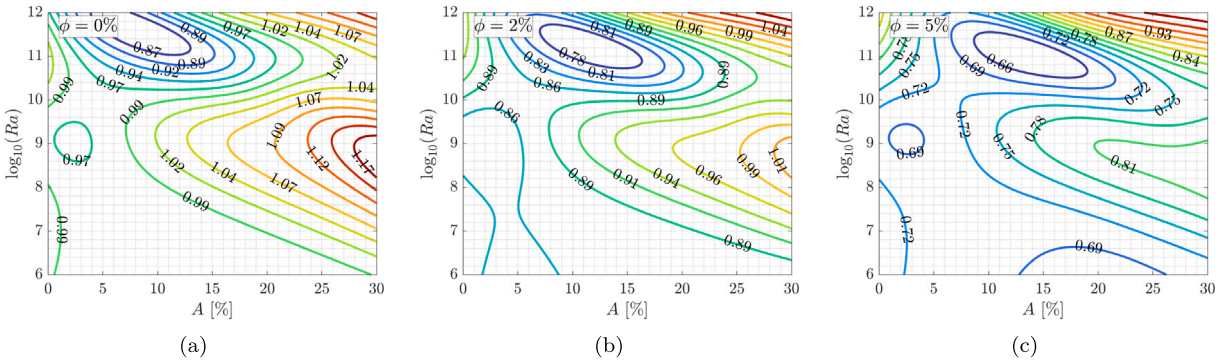

Fig. 14. Contours of thermal efficiency $\eta = E/E0$ as functions of Ra and A for $\phi = 0\%$ to 5%, based on ANN predictions.

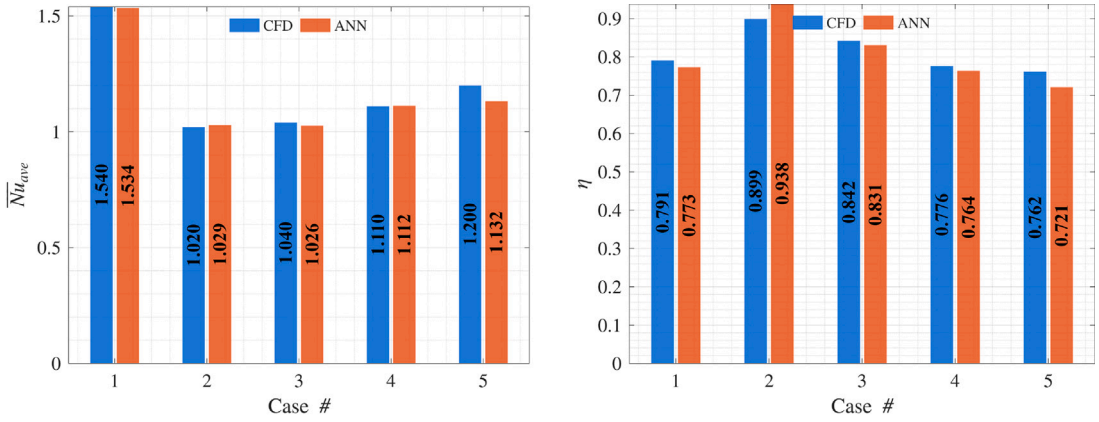

$$\textbf{Case 1} = \begin{cases} A = 9.38 \\ Ra = 10^{10.03} \\ \phi = 3.48 \end{cases} \quad \textbf{Case 2} = \begin{cases} A = 2.97 \\ Ra = 10^{7.53} \\ \phi = 1.12 \end{cases} \quad \textbf{Case 3} = \begin{cases} A = 1.03 \\ Ra = 10^{8.78} \\ \phi = 2.12 \end{cases} \quad \textbf{Case 4} = \begin{cases} A = 5.43 \\ Ra = 10^{8.05} \\ \phi = 3.04 \end{cases} \quad \textbf{Case 5} = \begin{cases} A = 4.06 \\ Ra = 10^{9.67} \\ \phi = 3.89 \end{cases}$$

Fig. 15. Comparison of the $\overline{Nu}_{ave}$ and thermal efficiency between CFD simulations and artificial neural network predictions.

time-consuming simulations. To enable a more rigorous comparison and to assess the validity of the ANN results, we designed a framework in which the design parameters the Rayleigh number, ϕ, and A were randomly sampled. For each parameter set, a CFD simulation was performed, and its outputs were compared against the previously generated ANN predictions. This process is performed for five cases. As shown in Fig. 15, the ANN closely reproduces the CFD trends for both $\overline{Nu}_{ave}$ and η across all five cases. The discrepancies are small typically a few percent and the average error of all cases are below 2%, with the closest agreement observed at moderate parameter values. Overall, these results confirm that the trained ANN preserves the absolute levels and case-wise ranking of the metrics, providing a relative accurate and cost-efficient surrogate for rapid evaluations over the design space.

5. Conclusion

This study conducted a comprehensive three-dimensional numerical investigation of steady-state natural convection within an open-ended cubic enclosure featuring a wavy heated wall and filled with ternary hybrid nanofluid composed of H_2O, Cu, CuO, and Al_2O_3 nanoparticles. Utilizing the RANS framework along with the realizable k–ε turbulence model, the impacts of Rayleigh number ($10^6 \leq Ra \leq 10^{12}$), nanoparticle volume fraction ($0\% \leq \phi \leq 5\%$), and wall waviness amplitude ($0\% \leq$

$A \leq 30\%$) were systematically evaluated on thermal performance, flow structure, and entropy generation. The results revealed that increasing the wall waviness amplitude significantly enhances convective mixing by disturbing thermal boundary layers and generating secondary flow structures. This leads to substantial augmentation in both local and average Nusselt numbers ($\overline{Nu}_{ave}$). For instance, at $Ra = 10^{10}$ and $\phi = 5\%$, increasing A from 0% to 30% increased $\overline{Nu}_{ave}$ from approximately 1.13 to 2.65, indicating a relative enhancement of over 134%. The addition of nanoparticles improved the effective thermal conductivity of the base fluid, but higher concentrations also increased the dynamic viscosity, resulting in additional flow resistance. Nevertheless, this adverse effect was mitigated by the enhanced circulation due to wall oscillations. An optimal nanoparticle loading of $\phi = 2\%$ was identified, delivering high thermal enhancement while maintaining flow efficiency. Moreover, the analysis of thermal entropy generation demonstrated that wall waviness amplitudes of $A \geq 20\%$ substantially reduced irreversibilities, especially under turbulent regimes. For example, the normalized thermal efficiency at $Ra = 10^{12}$ improved from approximately 0.78 (for $\phi = 5\%$, $A = 0\%$) to 1.08 when A was increased to 30%, highlighting the synergistic effect of geometrical modulation and nanoparticle presence. This trend was particularly evident for moderate nanoparticle concentrations. To extend the practical applicability of the findings, an ANN model was developed and trained on the CFD dataset to predict $\overline{Nu}_{ave}$ and η across the parametric domain. The model achieved a high prediction accuracy with a correlation coefficient of $R^2 = 0.99992$ over the testing data, suggesting its potential as a fast and reliable surrogate for design optimization. In summary, the study provides valuable insights into the coupled effects of nanofluid thermophysical properties and passive geometrical modifications on buoyancy-driven convective systems. It demonstrates that combining ternary hybrid nanofluids with surface undulations offers a powerful approach to enhance thermal performance significantly. These findings have practical implications in the design of compact and efficient thermal management systems in applications such as electronic cooling, energy harvesting devices, and next-generation heat exchangers. And also it should be noted that the results and discussions of the present study are limited to cubic 3D cavities with uniform wall dimensions, a sinusoidal corrugated wall profile, and the investigated Rayleigh number range of $Ra = 10^6$ to 10^{12}.

CRediT authorship contribution statement

Mohammad Abbaszadeh: Validation, Software, Methodology, Investigation, Conceptualization. **Alireza Timas:** Writing – review & editing, Writing – original draft, Visualization, Data curation. **Mohammad Ghalambaz:** Writing – review & editing, Supervision.

Declaration of competing interest

The authors declare that they have no known competing financial interests or personal relationships that could have appeared to influence the work reported in this paper.

Data availability

Data will be made available on request.

References

[1] M. Piratheepan, T. Anderson, Natural convection heat transfer in façade integrated solar concentrators, Sol. Energy 122 (2015) 271–276, http://dx.doi.org/10.1016/j.solener.2015.09.008, URL: https://www.sciencedirect.com/science/article/pii/S0038092X15004892.

[2] C. Lei, Y. Zhu, S. Qiu, C. Wang, R. Bao, C. Deng, Characteristics of natural convection heat transfer in composite cavity, Case Stud. Therm. Eng. 56 (2024) 104254, http://dx.doi.org/10.1016/j.csite.2024.104254, URL: https://www.sciencedirect.com/science/article/pii/S2214157X24002855.

[3] P.R. Santos, A.T. Franco, S.L. Junqueira, Numerical investigation of viscoplastic fluids on natural convection in open cavities with solid obstacles, Heliyon 10 (4) (2024) e26243, http://dx.doi.org/10.1016/j.heliyon.2024.e26243, URL: https://www.sciencedirect.com/science/article/pii/S2405844024022746.

[4] R.D. Selvakumar, D. Zhonglin, J. Wu, Heat transfer intensification by EHD conduction pumping for electronic cooling applications, Int. J. Heat Fluid Flow 95 (2022) 108972, http://dx.doi.org/10.1016/j.ijheatfluidflow.2022.108972, URL: https://www.sciencedirect.com/science/article/pii/S0142727X22000479.

[5] Y. Li, Q. Yu, S. Yu, P. Zhang, J. Zhang, Numerical investigation and mechanism analysis of heat transfer enhancement in a helical tube by square wave pulsating flow, Heat Mass Transf. 59 (1) (2023) 21–37.

[6] B. Bian, D. Dovizio, W. Villanueva, Direct numerical simulation of internally heated natural convection in a hemispherical geometry, Int. J. Heat Mass Transfer 220 (2024) 124997, http://dx.doi.org/10.1016/j.ijheatmasstransfer.2023.124997, URL: https://www.sciencedirect.com/science/article/pii/S0017931023011420.

[7] M. Rogowski, R. Andrzejczyk, Recent advances of selected passive heat transfer intensification methods for phase change material-based latent heat energy storage units: A review, Int. Commun. Heat Mass Transfer 144 (2023) 106795, http://dx.doi.org/10.1016/j.icheatmasstransfer.2023.106795, URL: https://www.sciencedirect.com/science/article/pii/S0735193323001847.

[8] P. Murugesan, K. Mayilsamy, S. Suresh, Turbulent heat transfer and pressure drop in tube fitted with square-cut twisted tape, Chin. J. Chem. Eng. 18 (4) (2010) 609–617, http://dx.doi.org/10.1016/S1004-9541(10)60264-9, URL: https://www.sciencedirect.com/science/article/pii/S1004954110602649.

[9] S. Eiamsa-ard, P. Promthaisong, C. Thianpong, M. Pimsarn, V. Chuwattanakul, Influence of three-start spirally twisted tube combined with triple-channel twisted tape insert on heat transfer enhancement, Chem. Eng. Process.: Process. Intensif. 102 (2016) 117–129, http://dx.doi.org/10.1016/j.cep.2016.01.012, URL: https://www.sciencedirect.com/science/article/pii/S0255270116300125.

[10] M. Mellal, R. Benzeguir, D. Sahel, H. Ameur, Hydro-thermal shell-side performance evaluation of a shell and tube heat exchanger under different baffle arrangement and orientation, Int. J. Therm. Sci. 121 (2017) 138–149, http://dx.doi.org/10.1016/j.ijthermalsci.2017.07.011, URL: https://www.sciencedirect.com/science/article/pii/S1290072917302053.

[11] A. El Maakoul, A. Laknizi, S. Saadeddine, A. Ben Abdellah, M. Meziane, M. El Metoui, Numerical design and investigation of heat transfer enhancement and performance for an annulus with continuous helical baffles in a double-pipe heat exchanger, Energy Convers. Manage. 133 (2017) 76–86, http://dx.doi.org/10.1016/j.enconman.2016.12.002, URL: https://www.sciencedirect.com/science/article/pii/S0196890416310780.

[12] S. Ahmad, Y. ul Umair Bin Turabi, D. Liu, H. Waqas, S. Munir, Numerical simulation of magnetohydrodynamics double-diffusive natural convection in a cavity with non-uniform heated walls, Appl. Therm. Eng. 253 (2024) 123778, http://dx.doi.org/10.1016/j.applthermaleng.2024.123778, URL: https://www.sciencedirect.com/science/article/pii/S1359431124014467.

[13] A.J. Modi, N.A. Kalel, M.K. Rathod, Thermal performance augmentation of fin-and-tube heat exchanger using rectangular winglet vortex generators having circular punched holes, Int. J. Heat Mass Transfer 158 (2020) 119724, http://dx.doi.org/10.1016/j.ijheatmasstransfer.2020.119724, URL: https://www.sciencedirect.com/science/article/pii/S0017931020303689.

[14] C. Gnanavel, R. Saravanan, M. Chandrasekaran, Heat transfer enhancement through nano-fluids and twisted tape insert with rectangular cut on its rib in a double pipe heat exchanger, Mater. Today: Proc. 21 (2020) 865–869, http://dx.doi.org/10.1016/j.matpr.2019.07.606, URL: https://www.sciencedirect.com/science/article/pii/S2214785319328019. International Conference on Recent Trends in Nanomaterials for Energy, Environmental and Engineering Applications.

[15] M. Abbaszadeh, M.H. Montazeri, M. Mirzaie, Heat transfer and thermal efficiency enhancement using twisted tapes in sinusoidal wavy tubes with nanofluids: a numerical study, Internat. J. Numer. Methods Heat Fluid Flow 33 (12) (2023) 4062–4089, http://dx.doi.org/10.1108/HFF-06-2023-0331, URL: https://www.emerald.com/hff/article-abstract/33/12/4062/191687/Heat-transfer-and-thermal-efficiency-enhancement.

[16] E. Bilgen, A. Muftuoglu, Natural convection in an open square cavity with slots, Int. Commun. Heat Mass Transfer 35 (8) (2008) 896–900, http://dx.doi.org/10.1016/j.icheatmasstransfer.2008.05.001, URL: https://www.sciencedirect.com/science/article/pii/S0735193308001012.

[17] É. Fontana, A. da Silva, V.C. Mariani, Natural convection in a partially open square cavity with internal heat source: An analysis of the opening mass flow, Int. J. Heat Mass Transfer 54 (7) (2011) 1369–1386, http://dx.doi.org/10.1016/j.ijheatmasstransfer.2010.11.053, URL: https://www.sciencedirect.com/science/article/pii/S0017931010006812.

[18] M.M. Elsayed, N.M. Al-Najem, M.M. El-Refaee, A.A. Noor, Numerical study of natural convection in fully open tilted cavities, Heat Transf. Eng. 20 (3) (1999) 73–85, http://dx.doi.org/10.1080/014576399271448, arXiv:https://doi.org/10.1080/014576399271448.

[19] R. Abhinav, P.S. Sunder, A. Gowrishankar, S. Vignesh, M. Vivek, V.R. Kishore, Numerical study on effect of vent locations on natural convection in an enclosure with an internal heat source, Int. Commun. Heat Mass Transfer 49 (2013)

69–77, http://dx.doi.org/10.1016/j.icheatmasstransfer.2013.09.001, URL: https://www.sciencedirect.com/science/article/pii/S0735193313001863.

[20] A.K. Hussein, A.W. Mustafa, Natural convection in fully open parallelogrammic cavity filled with Cu–water nanofluid and heated locally from its bottom wall, Therm. Sci. Eng. Prog. 1 (2017) 66–77, http://dx.doi.org/10.1016/j.tsep.2017.03.002, URL: https://www.sciencedirect.com/science/article/pii/S2451904916300427.

[21] O. Polat, E. Bilgen, Laminar natural convection in inclined open shallow cavities, Int. J. Therm. Sci. 41 (4) (2002) 360–368, http://dx.doi.org/10.1016/S1290-0729(02)01326-1, URL: https://www.sciencedirect.com/science/article/pii/S1290072902013261.

[22] P.R. Santos, A.T. Franco, S.L. Junqueira, M. Nadeem, Natural convection of viscoplastic fluids in side-heated open cavities, Case Stud. Therm. Eng. 73 (2025) 106689, http://dx.doi.org/10.1016/j.csite.2025.106689, URL: https://www.sciencedirect.com/science/article/pii/S2214157X25009499.

[23] G. Biswal, G.S. Meshram, Computational investigation of aspect ratio and inclination effects on natural convection heat transfer in nanofluid-filled rough wall cavities, Numer. Heat Transf. Part A: Appl. 86 (11) (2025) 3514–3529, http://dx.doi.org/10.1080/10407782.2024.2302077, arXiv:https://doi.org/10.1080/10407782.2024.2302077.

[24] K.M. Gangawane, R.P. Bharti, S. Kumar, Lattice Boltzmann analysis of natural convection in a partially heated open ended enclosure for different fluids, J. Taiwan Inst. Chem. Eng. 49 (2015) 27–39, http://dx.doi.org/10.1016/j.jtice.2014.11.020, URL: https://www.sciencedirect.com/science/article/pii/S1876107014003836.

[25] A. Sanjari, M. Abbaszadeh, A. Abbassi, Lattice Boltzmann simulation of free convection in an inclined open-ended cavity partially filled with fibrous porous media, J. Porous Media 21 (12) (2018) 1265–1281, http://dx.doi.org/10.1615/JPorMedia.2018028755, URL: https://www.dl.begellhouse.com/journals/49dcde6d4c0809db,429a4b3f20e10c6a,6b71908379fc1b3f.html.

[26] G.S. Meshram, G. Biswal, Exploration of heat transfer and entropy generation in an irregular wall cavity filled with Al2O3-water nanofluid, Numer. Heat Transf. Part A: Appl. (2024) 1–22, http://dx.doi.org/10.1080/10407782.2024.2372707, arXiv:https://doi.org/10.1080/10407782.2024.2372707.

[27] M. Jelita, H. Saleh, Comparative analysis of heat transfer performance in cavities with varied wall conditions and nano encapsulated phase change material–water, J. Energy Storage 95 (2024) 112532, http://dx.doi.org/10.1016/j.est.2024.112532, URL: https://www.sciencedirect.com/science/article/pii/S2352152X24021182.

[28] A. Alazzam, N.A. Qasem, A. Aissa, M.S. Abid, K. Guedri, O. Younis, Natural convection characteristics of nano-encapsulated phase change materials in a rectangular wavy enclosure with heating element and under an external magnetic field, J. Energy Storage 57 (2023) 106213, http://dx.doi.org/10.1016/j.est.2022.106213, URL: https://www.sciencedirect.com/science/article/pii/S2352152X22022022.

[29] M.S. Hasan, M.N. Alam, M. Sarker, MHD convective thermal performance in a nanofluid-filled wavy enclosure: an artificial neural network model, Int. J. Thermofluids (2025) 101186, http://dx.doi.org/10.1016/j.ijft.2025.101186, URL: https://www.sciencedirect.com/science/article/pii/S2666202725001338.

[30] S. Hansda, S.K. Pandit, T.W.H. Sheu, Thermosolutal discharge of double diffusion mixed convection flow with Brownian motion of nanoparticles in a wavy chamber, J. Therm. Anal. Calorim. 147 (12) (2022) 7007–7029, http://dx.doi.org/10.1007/s10973-021-10971-4.

[31] C. Kleinstreuer, Y. Feng, Experimental and theoretical studies of nanofluid thermal conductivity enhancement: a review, Nanoscale Res. Lett. 6 (2011) 1–13.

[32] S. Hansda, S.K. Pandit, On the analysis of thermosolutal mixed convection in differentially heated and soluted geometries beyond rectangular, Internat. J. Numer. Methods Heat Fluid Flow 33 (8) (2023) 2877–2901, http://dx.doi.org/10.1108/HFF-12-2022-0718.

[33] H. Sayyou, J. Belabid, H.F. Öztop, K. Allali, Vibrational effects on thermosolutal free convection of Cu-Al2O3/water nanofluids in a partially heated and salted square porous enclosure, J. Mol. Liq. 423 (2025) 126990, http://dx.doi.org/10.1016/j.molliq.2025.126990, URL: https://www.sciencedirect.com/science/article/pii/S0167732225001485.

[34] D. Li, H. Zhang, P. Ye, Z. Yu, Natural convection of power-law nanofluid in a square enclosure with a circular cylinder: An immersed boundary-lattice Boltzmann study, Internat. J. Modern Phys. C 29 (11) (2018) 1850105, http://dx.doi.org/10.1142/S012918311850105X, arXiv:https://doi.org/10.1142/S012918311850105X.

[35] J. Hossain, B.K. Mondal, S.K. Mostaque, Computational investigation on the photovoltaic performance of an efficient GeSe-based dual-heterojunction thin film solar cell, Semicond. Sci. Technol. 37 (1) (2021) 015008, http://dx.doi.org/10.1088/1361-6641/ac30e9.

[36] A. Hossain, M.M. Molla, MHD mixed convection of non-Newtonian power-law ferrofluid in a wavy enclosure, J. Therm. Anal. Calorim. 148 (21) (2023) 11871–11892.

[37] P. Rana, A. Kumar, G. Gupta, Impact of different arrangements of heated elliptical body, fins and differential heater in MHD convective transport phenomena of inclined cavity utilizing hybrid nanoliquid: Artificial neutral network prediction, Int. Commun. Heat Mass Transfer 132 (2022) 105900, http://dx.doi.org/10.1016/j.icheatmasstransfer.2022.105900, URL: https://www.sciencedirect.com/science/article/pii/S0735193322000227.

[38] A. Li, A.C.Y. Yuen, W. Wang, T.B.Y. Chen, C.S. Lai, W. Yang, W. Wu, Q.N. Chan, S. Kook, G.H. Yeoh, Integration of computational fluid dynamics and artificial neural network for optimization design of battery thermal management system, Batteries 8 (7) (2022) http://dx.doi.org/10.3390/batteries8070069, URL: https://www.mdpi.com/2313-0105/8/7/69.

[39] S. Panda, S. Ontela, S.R. Mishra, T. Thumma, Hybridization of artificial neural network and response surface methodology for the optimized heat transfer rate on three-dimensional micropolar nanofluid using Hamilton–Crosser conductivity model through a circular cylinder, J. Therm. Anal. Calorim. 148 (17) (2023) 9027–9046, http://dx.doi.org/10.1007/s10973-023-12283-1.

[40] F. Wang, R. Parveen, S. Rehman, A. Farooq, H. Alhazmi, A. Aljohani, I. Khan, A.S. Omer, Artificial neural computing and statistical analysis of heat and mass transport of nanofluid flow with melting heat and thermal stratification, Case Stud. Therm. Eng. 60 (2024) 104563, http://dx.doi.org/10.1016/j.csite.2024.104563, URL: https://www.sciencedirect.com/science/article/pii/S2214157X2400594X.

[41] H.S. Sultan, M.H. Ali, J. Shafi, M. Fteiti, M. Baro, F. Alresheedi, M.S. Islam, T. Yusaf, M. Ghalambaz, Improving phase change heat transfer in an enclosure filled by uniform and heterogenous metal foam layers: A neural network design approach, J. Energy Storage 85 (2024) 110954, http://dx.doi.org/10.1016/j.est.2024.110954, URL: https://www.sciencedirect.com/science/article/pii/S2352152X24005383.

[42] H.S.S. Aljibori, M.H. Ali, Z. Raizah, A. Hajjar, J. Shafi, F. Alresheedi, A. Elhassanein, M. Edalatifar, M. Ghalambaz, An artificial intelligence – Finite element study of magnetohydrodynamic heat transfer of a nano-encapsulated phase change material suspension in a cylindrical enclosure with partial heated walls, Int. Commun. Heat Mass Transfer 164 (2025) 108812, http://dx.doi.org/10.1016/j.icheatmasstransfer.2025.108812, URL: https://www.sciencedirect.com/science/article/pii/S0735193325002374.

[43] S. Cengizci, H.F. Öztop, G. Mülayim, Stabilized finite element simulation of natural convection in square cavities filled with nanofluids under various temperature boundary conditions, Int. Commun. Heat Mass Transfer 156 (2024) 107655, http://dx.doi.org/10.1016/j.icheatmasstransfer.2024.107655, URL: https://www.sciencedirect.com/science/article/pii/S0735193324004172.

[44] D.K. Mandal, M.K. Mondal, N. Biswas, N.K. Manna, K. Al-Farhany, A. Mitra, A.J. Chamkha, Convective heat transport in a porous wavy enclosure: Nonuniform multi-frequency heating with hybrid nanofluid and magnetic field, Heliyon 10 (9) (2024) e29846, http://dx.doi.org/10.1016/j.heliyon.2024.e29846, URL: https://www.sciencedirect.com/science/article/pii/S2405844024058778.

[45] H.S. Sultan, M.H. Ali, J. Shafi, M. Fteiti, M. Baro, K. Almutairi, M.S. Islam, K. Harb, F.S. Alharbi, M. Ghalambaz, Design improvement of latent heat thermal energy storage in wavy channel enclosures using neural networks, J. Energy Storage 79 (2024) 110061, http://dx.doi.org/10.1016/j.est.2023.110061, URL: https://www.sciencedirect.com/science/article/pii/S2352152X23034606.

[46] R. Roslan, H. Saleh, I. Hashim, Buoyancy-driven heat transfer in nanofluid-filled trapezoidal enclosure with variable thermal conductivity and viscosity, Numer. Heat Transf. Part A: Appl. 60 (10) (2011) 867–882, http://dx.doi.org/10.1080/10407782.2011.616778, arXiv:https://doi.org/10.1080/10407782.2011.616778.

[47] M. Turkyilmazoglu, Unsteady convection flow of some nanofluids past a moving vertical flat plate with heat transfer, J. Heat Transf. 136 (3) (2013) 031704, http://dx.doi.org/10.1115/1.4025730.

[48] M. Goodarzi, M. Safaei, K. Vafai, G. Ahmadi, M. Dahari, S. Kazi, N. Jomhari, Investigation of nanofluid mixed convection in a shallow cavity using a two-phase mixture model, Int. J. Therm. Sci. 75 (2014) 204–220, http://dx.doi.org/10.1016/j.ijthermalsci.2013.08.003, URL: https://www.sciencedirect.com/science/article/pii/S1290072913001920.

[49] B. Zamora, Determining correlations for solar chimneys in buildings with wind interference: A numerical approach, Sustain. Energy Technol. Assess. 48 (2021) 101662, http://dx.doi.org/10.1016/j.seta.2021.101662, URL: https://www.sciencedirect.com/science/article/pii/S2213138821006767.

[50] A. Haghiri, X. Xu, R.D. Sandberg, K. Tanimoto, T. Oda, Improving a two-equation eddy-viscosity turbulence model for high-Rayleigh-number natural-convection flows using machine learning, J. Eng. Gas Turbines Power 147 (1) (2024) 011026, http://dx.doi.org/10.1115/1.4066594.

[51] H.-T. Chen, S.-H. Wang, S. Rashidi, W.-M. Yan, Study on three-dimensional natural convection heat transfer in a house with two heating surfaces, J. Therm. Anal. Calorim. 149 (22) (2024) 13175–13197, http://dx.doi.org/10.1007/s10973-024-13521-w.

[52] P. Huang, J. Bardina, T. Coakley, Turbulence modeling validation, testing, and development, NASA Tech. Memo. 110446 (1997) 10–2514.

[53] K. Alqawasmi, K.A.M. Alharbi, U. Farooq, S. Noreen, M. Imran, A. Akgül, M. Kanan, J. Asad, Numerical approach toward ternary hybrid nanofluid flow with nonlinear heat source-sink and fourier heat flux model passing through a disk, Int. J. Thermofluids 18 (2023) 100367, http://dx.doi.org/10.1016/j.ijft.2023.100367, URL: https://www.sciencedirect.com/science/article/pii/S266620272300085X.

[54] M. Ramzan, N. Shahmir, I. Alazman, C.V.A. Saleel, J.M. Asiri, A.M. Saeed, W.S. Koh, Heat transfer performance appraisal of hybrid and ternary nanofluid flows over a wedge considering viscous dissipation and quadratic thermal convection: Non-similar solution approach, Adv. Mech. Eng. 17 (6) (2025) 16878132251349955, http://dx.doi.org/10.1177/16878132251349955, arXiv:https://doi.org/10.1177/16878132251349955.

[55] K. Batool, G.A. Khouqeer, S. Zainab, N. AbdelAll, F. Haq, M. Sallah, Physical aspects of heat transfer in ternary hybrid nanofluid flow subject to induced magnetic field and Cattaneo–Christov heat flux, Int. J. Energy Res. 2025 (1) (2025) 5510496, http://dx.doi.org/10.1155/er/5510496, URL: https://onlinelibrary.wiley.com/doi/abs/10.1155/er/5510496, arXiv:https://onlinelibrary.wiley.com/doi/pdf/10.1155/er/5510496.

[56] S.L. Yadav, A.K. Singh, et al., Analysis of entropy generation in a rectangular porous duct, J. Appl. Math. Phys. 4 (07) (2016) 1336.

[57] A. Mohamad, M. El-Ganaoui, R. Bennacer, Lattice Boltzmann simulation of natural convection in an open ended cavity, Int. J. Therm. Sci. 48 (10) (2009) 1870–1875, http://dx.doi.org/10.1016/j.ijthermalsci.2009.02.004, URL: https://www.sciencedirect.com/science/article/pii/S1290072909000313.

[58] M. Jahanshahi, S. Hosseinizadeh, M. Alipanah, A. Dehghani, G. Vakilinejad, Numerical simulation of free convection based on experimental measured conductivity in a square cavity using Water/SiO2 nanofluid, Int. Commun. Heat Mass Transfer 37 (6) (2010) 687–694, http://dx.doi.org/10.1016/j.icheatmasstransfer.2010.03.010, URL: https://www.sciencedirect.com/science/article/pii/S0735193310000722.

[59] A. Alklaibi, K.V.C. Mouli, L.S. Sundar, Heat transfer, and friction factor of Fe3O4–SiO2/Water hybrid nanofluids in a plate heat exchanger: Experimental and ANN predictions, Int. J. Therm. Sci. 195 (2024) 108608, http://dx.doi.org/10.1016/j.ijthermalsci.2023.108608, URL: https://www.sciencedirect.com/science/article/pii/S1290072923004696.

[60] K.U. Rehman, W.A. Shatanawi, T.A.M. Shatnawi, Machine learning based analysis of heat transfer in tangent hyperbolic fluid at heat generating magnetized surface, Int. J. Thermofluids (2024) URL: https://api.semanticscholar.org/CorpusID:267168969.

[61] Y.M. Seo, K. Luo, M.Y. Ha, Y.G. Park, Direct numerical simulation and artificial neural network modeling of heat transfer characteristics on natural convection with a sinusoidal cylinder in a long rectangular enclosure, Int. J. Heat Mass Transfer 152 (2020) 119564, http://dx.doi.org/10.1016/j.ijheatmasstransfer.2020.119564, URL: https://www.sciencedirect.com/science/article/pii/S001793101935481X.